Journal of Computational Physics **165,** 354–406 (2000)
doi:10.1006/jcph.2000.6614, available online at http://www.idealibrary.com on IDEAL®

Vortex Methods for High-Resolution Simulations of Viscous Flow Past Bluff Bodies of General Geometry

P. Ploumhans and G. S. Winckelmans

Center for Systems Engineering and Applied Mechanics, Department of Mechanical Engineering, Université catholique de Louvain, 1348 Louvain-la-Neuve, Belgium
E-mail: ploumhan@term.ucl.ac.be, gsw@term.ucl.ac.be

Received August 3, 1999; revised March 15, 2000; published online November 16, 2000

Recent contributions to the 2-D vortex method are presented. A technique to accurately redistribute particles in the presence of bodies of general geometry is developed. The particle strength exchange (PSE) scheme for diffusion is modified for particles in the vicinity of the solid boundaries to avoid a spurious vorticity flux during the convection/PSE step. The scheme used to enforce the no-slip condition through the vorticity flux at the boundary is modified in a way that is more accurate than in the previous method. Finally, to perform simulations with nonuniform resolution, a mapping of the redistribution lattice is also used. In that case, the PSE is still done in the physical domain, using a symmetrized, conservative scheme. The quadratic convergence of this scheme is proved mathematically, and numerical tests are shown to support the proof. These elements are all validated on the benchmark problem of the flow past an impulsively started cylinder. High-resolution, long-time simulations of the flow past other bluff bodies are also presented: the case of a square and of a capsule at angle of attack.

Key Words: vortex methods; viscous flow; particle redistribution; general geometry.

1. INTRODUCTION

In the past two decades, there have been significant developments in the field of vortex methods: fast algorithms using multipole expansions (Greengard and Rohklin [6], Barnes and Hut [2]) and active error control (Salmon and Warren [16], Winckelmans *et al.* [19, 20]), accurate treatment of viscous effects using the particle strength exchange scheme (PSE, Degond and Mas-Gallic [5]), and accurate enforcement of the viscous boundary condition (Koumoutsakos *et al.* [8], Mas-Gallic [14a], Leonard *et al.* [12], Ploumhans *et al.* [15], Benhaddouch [2a]). These elements have made the vortex method suitable for the computation of high-resolution simulations of flows with viscous boundaries. For instance, such

0021-9991/00 $35.00

computations were carried out by Koumoutsakos and Leonard [9] and by Koumoutsakos and Shiels [10], who used the method to study impulsively started flows past a cylinder and past a flat plate, respectively. So far, accurate simulations have only been achieved for flows past bodies of particular geometry (e.g., the circular cylinder, the flat plate). Recently, the use of a mapping was introduced in the vortex methods, allowing one to perform simulations with nonuniform spatial resolution (Cottet *et al.* [3], Lemine [11], and Cottet and Koumoutsakos [4]).

In this paper, we present several new contributions to vortex methods aimed at the high-resolution computation of flows past bluff bodies of general geometry. We also combine these developments with the use of a mapping to perform simulations with nonuniform spatial resolution. In this case, the PSE is modified and is still done in physical space.

The paper is organized into the following parts: The basic equations (Section 2), the 2-D vortex method with its new developments (Section 3), the validation of these new developments for the flow past an impulsively started circular cylinder at uniform (Section 4) and nonuniform (Section 5) resolutions, the computation of the flow past a square using two different nonuniform resolutions (Section 6), the simulation of the flow past a body of nontrivial geometry (Section 7), and a simple approach to particle redistribution in the presence of a body (Section 8). Appendix A provides the mathematical proof that the modified PSE is convergent, and Appendix B provides numerical tests that support the proof.

2. THE BASIC EQUATIONS FOR 2-D FLOWS

Two-dimensional incompressible flows are governed by the vorticity equation

$$\frac{D\omega}{Dt} = \frac{\partial \omega}{\partial t} + \mathbf{u} \cdot \nabla \omega = \nu \nabla^2 \omega, \tag{1}$$

where $\mathbf{u}(\mathbf{x}, t)$ is the velocity field, ν is the kinematic viscosity, and $\boldsymbol{\omega} = \nabla \times \mathbf{u} = \omega \cdot \mathbf{e}_z$ is the vorticity. In bluff-body flows, with the body translating with velocity $\mathbf{U}_b(t)$ and rotating around its center of mass, $\mathbf{x}_b$, with angular velocity $\Omega(t)$, the fluid velocity on the body surface, $\mathbf{x}_s$, is equal to the velocity of the body, $\mathbf{U}_s$:

$$\mathbf{u}(\mathbf{x}_s) = \mathbf{U}_s = \mathbf{U}_b(t) + \mathbf{e}_z \times (\mathbf{x}_s - \mathbf{x}_b)\Omega_b(t). \tag{2}$$

At infinity, we have

$$\mathbf{u}(\mathbf{x}) \to \mathbf{U}_\infty \quad \text{as} \quad |\mathbf{x}| \to \infty, \tag{3}$$

with $\mathbf{U}_\infty$ the freestream velocity. For incompressible flows, the velocity can be expressed as

$$\mathbf{u} = \nabla \times \boldsymbol{\psi} + \mathbf{U}_\infty \tag{4}$$

with $\boldsymbol{\psi} = \psi \cdot \mathbf{e}_z$ the stream function related to $\boldsymbol{\omega}$ by

$$\nabla^2 \psi = -\omega. \tag{5}$$

3. THE VORTEX METHOD FOR 2-D FLOWS

The vorticity field is represented by N Lagrangian, scalar-valued, particles:

$$\omega(\mathbf{x}, t) = \sum_{i=1}^{N} \zeta_i(\mathbf{x} - \mathbf{x}_i)\Gamma_i. \tag{6}$$

Each particle is characterized by its position, $\mathbf{x}_i(t)$, and its strength, $\Gamma_i(t)$, i.e., its circulation, $\Gamma_i = \int_{S_i} \omega \, dS \triangleq \omega_i S_i$, with S_i the area of fluid associated with the particle i. The distribution function, ζ_i, associated with a particle is defined by

$$\zeta_i(\mathbf{x}) = \frac{1}{\sigma_i^2}\,\zeta\left(\frac{|\mathbf{x}|}{\sigma_i}\right) \tag{7}$$

with σ_i the smoothing parameter. There are many possible choices for the function ζ (see, e.g., Leonard [14], Winckelmans and Leonard [18]). In this paper, the Gaussian distribution is used throughout:

$$\zeta(\rho) = \frac{1}{2\pi}\exp\left(-\frac{\rho^2}{2}\right). \tag{8}$$

The velocity at any position $\mathbf{x}$, computed from ω (Biot–Savart law), is

$$\mathbf{u}(\mathbf{x}, t) = -\sum_{j=1}^{N} \frac{q(|\mathbf{x} - \mathbf{x}_j|/\sigma_j)}{|\mathbf{x} - \mathbf{x}_j|^2}\,(\mathbf{x} - \mathbf{x}_j) \times \mathbf{e}_z \Gamma_j \tag{9}$$

with $q(\rho) = \int_0^\rho \zeta(s) s \, ds (= \frac{1}{2\pi}(1 - \exp(-\rho^2/2))$ for the Gaussian smoothing).

The way to handle viscous boundaries in the vortex method was originally developped by Koumoutsakos *et al.* [8]. In the present paper, a modification of the method is presented that is more accurate and also better suited to the computation of flows past bodies of general geometry. A typical time step, Δt, of the vortex method is divided into two substeps.

- In *substep 1*, the local velocity is computed and integrated with a second-order Adams–Bashforth scheme to convect the particles (Section 3.1). Their strength is updated with a modified particle strength exchange scheme (Section 3.2) that is integrated with an Euler explicit scheme. This modified PSE guarantees a zero vorticity flux at the solid boundary during substep 1. After this substep, a slip velocity, $\Delta \mathbf{U}_{\text{slip}}$, is present at the solid boundary. Algorithmically, substep 1 is expressed as

$$\mathbf{x}_i^{n+1} = \mathbf{x}_i^n + \Delta t\left(\frac{3}{2}\mathbf{u}_i(\mathbf{x}^n, \Gamma^n) - \frac{1}{2}\mathbf{u}_i(\mathbf{x}^{n-1}, \Gamma^{n-1})\right) \tag{10}$$

$$\Gamma_i^* = \Gamma_i^n + \Delta t \left.\frac{d\Gamma_i}{dt}\right|_{\text{PSE}} (\mathbf{x}^n, \Gamma^n). \tag{11}$$

- In *substep 2*, the vortex sheet, $\Delta\gamma$, necessary on the body surface to cancel the slip velocity generated by substep 1, is computed (Section 3.3). This vortex sheet corresponds to a vorticity flux that must be emitted during a time Δt (Section 3.4):

$$\Gamma_i^{n+1} = \Gamma_i^* + \Delta t \left.\frac{d\Gamma_i}{dt}\right|_{\text{wall}} (\mathbf{x}^{n+1}, \Gamma^*). \tag{12}$$

Also, a redistribution scheme must be applied every few steps (Section 3.5) to maintain spatial uniformity of the particle distribution and thus maintain the second-order spatial accuracy of the method. After each particle redistribution, the new time step is done using a second-order Runge–Kutta scheme; substep 1 becomes

$$\mathbf{x}_i^{n+1/2} = \mathbf{x}_i^n + \Delta t\, \mathbf{u}_i(\mathbf{x}^n, \Gamma^n) \tag{13}$$

$$\Gamma_i^* = \Gamma_i^n + \Delta t \left.\frac{d\Gamma_i}{dt}\right|_{\mathrm{PSE}} (\mathbf{x}^n, \Gamma^n) \tag{14}$$

$$\mathbf{x}_i^{n+1} = \mathbf{x}_i^n + \frac{1}{2}\Delta t \left(\mathbf{u}_i(\mathbf{x}^n, \Gamma^n) + \mathbf{u}_i\left(\mathbf{x}^{n+1/2}, \Gamma^*\right)\right). \tag{15}$$

Substep 2 is still given by Eq. (12).

3.1. *Convection*

Particle positions, $\mathbf{x}_i(t)$, are governed by the equations

$$\frac{d}{dt}\mathbf{x}_i(t) = \mathbf{u}(\mathbf{x}_i(t), t), \quad 1 \le i \le N, \tag{16}$$

with

$$\mathbf{u}(\mathbf{x}_i(t), t) = -\sum_{j=1}^{N} \frac{q(|\mathbf{x}_i - \mathbf{x}_j|/\sigma_{ij})}{|\mathbf{x}_i - \mathbf{x}_j|^2} (\mathbf{x}_i - \mathbf{x}_j) \times \mathbf{e}_z \Gamma_j, \tag{17}$$

where $\sigma_{ij}^2 = (\sigma_i^2 + \sigma_j^2)/2$. The use of the symmetrized σ is needed for the convection step to conserve the moments of order 0, 1, and 2 of the vorticity field (Leonard [13]). The right-hand side of Eq. (17) is computed using a fast algorithm that has an operation count of $\mathcal{O}(N \log(N))$ and with active error control based on accurate error bounds (Barnes and Hut [2], Greengard and Rohklin [6], Salmon and Warren [16], Winckelmans *et al.* [19, 20]).

3.2. *Diffusion with Zero Flux at the Wall*

The treatment of diffusion is based on the technique of particle strength exchange (Degond and Mas-Gallic [5]). In this algorithm, the Laplacian operator ∇^2 is approximated by an integral operator,

$$\nabla^2\omega(\mathbf{x}) \approx \frac{2}{\sigma^2} \int \eta_\sigma(\mathbf{x} - \mathbf{y})\, (\omega(\mathbf{y}) - \omega(\mathbf{x}))\, d\mathbf{y}, \tag{18}$$

with $\eta_\sigma(\mathbf{x}) = (1/\sigma^2)\eta(|\mathbf{x}|/\sigma)$ and $\eta(s) = -\frac{1}{s}\frac{d}{ds}\zeta(s)$. The Gaussian smoothing is such that $\eta_\sigma = \zeta_\sigma$. The integral operator in Eq. (18) is discretized over the particles, and the evolution equation for the particle strengths becomes

$$\begin{aligned}\frac{d\Gamma_i}{dt} &= \frac{2\nu}{\sigma^2} \sum_{j=1}^{N} (S_i\Gamma_j - S_j\Gamma_i)\, \eta_\sigma(\mathbf{x}_i - \mathbf{x}_j) \\ &\simeq \frac{2\nu}{\sigma^2} \sum_{j \in \mathcal{P}_i} (S_i\Gamma_j - S_j\Gamma_i)\, \eta_\sigma(\mathbf{x}_i - \mathbf{x}_j)\,. \end{aligned} \tag{19}$$

In practice, the right-hand side of Eq. (19) does not involve a contribution from all N particles, as the rapid decrease of η means that only the particles close to particle i contribute significantly to $d\Gamma_i/dt$. The subset of particles that contribute significantly to $d\Gamma_i/dt$ is called $\mathcal{P}_i$. If the Gaussian smoothing is used, $\mathcal{P}_i$ consists, typically, of all the particles less than 5σ from $\mathbf{x}_i$. When σ is not the same for all particles, Eq. (19) is replaced by

$$\begin{aligned}\frac{d\Gamma_i}{dt} &= 2\nu \sum_{j=1}^{N} \frac{1}{\sigma_{ij}^2} (S_i\Gamma_j - S_j\Gamma_i)\, \eta_{ij}(\mathbf{x}_i - \mathbf{x}_j) \\ &\simeq 2\nu \sum_{j \in \mathcal{P}_i} \frac{1}{\sigma_{ij}^2} (S_i\Gamma_j - S_j\Gamma_i)\, \eta_{ij}(\mathbf{x}_i - \mathbf{x}_j) \end{aligned} \tag{20}$$

with $\eta_{ij}(\mathbf{x}_i - \mathbf{x}_j) = (1/\sigma_{ij}^2)\eta(|\mathbf{x}_i - \mathbf{x}_j|/\sigma_{ij})$. As for the original PSE [5], this symmetrized version of the PSE is still conservative: $\frac{d}{dt}(\sum_{i=1}^{N} \Gamma_i) = 0$. It is also still second-order accurate provided σ varies smoothly in space (see Appendixes A and B). An alternative approach is to do the PSE in a mapped domain as was done by Cottet *et al.* [3] and by Cottet and Koumoutsakos [4].

If Eq. (20) is used for wall-bounded computations, the PSE is not complete: Particles close to the wall are not completely surrounded by other particles. Consequently, a spurious vorticity flux appears at the wall (although the total vorticity is conserved). In order to complete the PSE, the present method uses image particles when computing the PSE for particles close to the wall. This zeroes the vorticity flux at the wall (see Benhaddouch [2a] for a modified PSE that allows one to enforce an arbitrary flux at the wall). Although numerical tests have not shown that images definitely improve the accuracy of the method, there are several reasons to use them:

- Early proofs of convergence of the vortex method in the presence of viscous boundaries require a zero vorticity flux at the boundary during substep 1 (Eqs. (11) and (14)); see Cottet and Koumoutsakos [4] and references therein.
- Images are necessary in 3-D to enforce the Dirichlet boundary condition on the normal component of the vorticity (Ploumhans *et al.* [15]).
- Having a zero vorticity flux during substep 1 allows one to easily compare the circulation produced by the vorticity flux on a part of the boundary for different methods (see Sections 4 and 5).

The use of images is first explained on a normalized 1-D problem (see Fig. 1). Consider a wall at $x = 0$. Particles are located at $x_j = j + \frac{1}{2}$ ($j \geq 0$) and have strength s_j. Image particles have position $x'_j = -x_j$ and strength $s'_j = s_j$. Figure 1 illustrates the effect of the

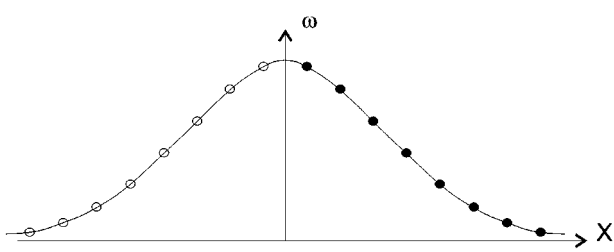

FIG. 1. Use of PSE images in 1-D: particles (●) and images (○).

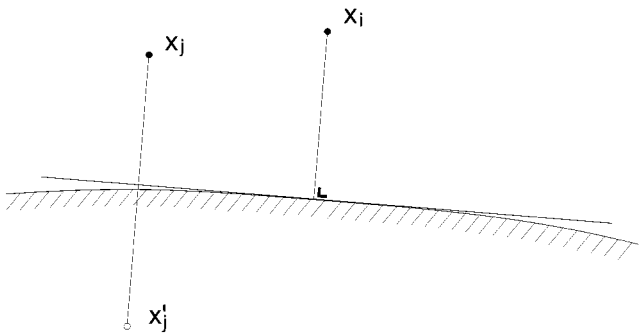

FIG. 2. Use of PSE images in 2-D.

image particles for the modified PSE: They guarantee zero vorticity flux at the wall. Also, because of the rapid decrease of η, the influence of the images is only felt by the particles close to the wall (typically, those with $x < 5$ if the Gaussian smoothing is used).

In 2-D, for obvious geometrical reasons, one cannot define a set of image particles as easily as in 1-D. The technique is therefore slightly different (see Fig. 2). The computation of the PSE for particle i involves two subsets of particles: $\mathcal{P}_i$ (the subset of particles *close enough* to $\mathbf{x}_i$) and $\mathcal{P}'_i$ (the set of the images of the particles in $\mathcal{P}_i$). If the particle i is such that $\mathbf{x}_i$ is more than d_{crit} (typically 5σ for the Gaussian smoothing) from the body surface, $\partial\mathcal{D}$, images have no effect on $d\Gamma_i/d$t; so $\mathcal{P}'_i$ is empty. If $\mathbf{x}_i$ is closer than d_{crit} from $\partial\mathcal{D}$, each particle in $\mathcal{P}_i$ has an image particle in $\mathcal{P}'_i$. If $\mathbf{x}_j$ is the position of a particle in $\mathcal{P}_i$, $\mathbf{x}'_j$ represents the position of its image. This position is computed using symmetry; with the axis of symmetry being the line tangent to $\partial\mathcal{D}$ that contains the point of $\partial\mathcal{D}$ closest to $\mathbf{x}_i$ (see Fig. 2). The strength (Γ'_j), surface (S'_j), and smoothing parameter (σ'_j) associated with an image particle are equal to those of the original particle. This technique is not affected by curvature effects as long as the curvature radius is much larger than $\sqrt{\nu\Delta t}$, which is the case in all well-resolved simulations (see Sections 4–7).

The 1-D image-modified PSE is conservative, as can be seen from Fig. 1. This result is comforting since such a modified PSE indeed solves

$$\frac{\partial\omega}{\partial t} = \nu\frac{\partial^2\omega}{\partial x^2} \quad \text{with} \quad \frac{\partial\omega}{\partial x} = 0 \quad \text{at} \quad x = 0. \tag{21}$$

The 2-D image-modified PSE should also be conservative. In practice, however, this is not strictly the case: The sum $\sum_{i=1}^{N} d\Gamma_i/$dt is not zero (although it is small compared to $(\frac{1}{N}\sum_{i=1}^{N}(d\Gamma_i/dt)^2)^{1/2}$. This calls for a correction that will be applied when the vortex sheet is computed (Section 3.3). In that way, the correction will only affect particles close to the wall, not the entire flow.

3.3. *Computation of the Vortex Sheet*

After we convect the particles with the local velocity and update their strength according to the modified PSE, there is a slip velocity, $\Delta\mathbf{U}_{\text{slip}}$, at the wall. The vortex sheet, $\Delta\gamma$, necessary on the body surface to cancel this slip velocity is then computed using the boundary element method. The body surface is discretized using M boundary elements (i.e., "vortex sheet panels"), each of size $O(h)$ (with h the typical distance between particles in the vicinity of the body) and each of uniform strength. For each computational panel on the

body, the slip velocity underneath that panel is taken as the average, over the panel, of the slip velocity induced by the freestream and by all vortex particles which, for this step only, are considered as point vortices (to ensure that all the vorticity is indeed outside of the body). In 2-D, this can be done directly from the Green's function integral for the velocity potential induced by the freestream and by the point vortices (Koumoutsakos [7]). It can also be evaluated numerically, by integrating, with some appropriate numerical quadrature (e.g., Gauss quadrature), the slip velocity obtained from the fast algorithm. This later approach, although slightly less accurate than the first one, has a direct extension to 3-D. Once the panel-averaged slip velocity, $\Delta\overline{\mathbf{U}}_{\text{slip}}$, has been evaluated for all panels, computing the panel strengths to cancel the slip velocity amounts to solving a linear system. This is so because, in addition to inducing a uniform tangential velocity underneath themselves (equal to $\mathbf{n} \times \mathbf{e}_z \Delta\gamma/2$), the panels also induce a tangential velocity on one another. Notice that the tangential velocity induced by one panel on another is also averaged over that panel, using the same numerical quadrature as above.

An integral constraint,

$$\oint \Delta\gamma(s)\, ds = -2A_B[\Omega(t+\Delta t) - \Omega(t)], \tag{22}$$

with A_B the surface of the body, has to be imposed on the strength of the vortex sheet (Koumoutsakos *et al.* [8]). If Eq. (22) is discretized on the panels, it becomes

$$\sum_{i=1}^{M} \Delta\gamma_i\, b_i = -2A_B[\Omega(t+\Delta t) - \Omega(t)], \tag{23}$$

with $\Delta\gamma_i$ the strength of panel i, and b_i its length. To take into account the fact that the image-modified PSE is not exactly conservative, Eq. (23) is here replaced by

$$\sum_{i=1}^{M} \Delta\gamma_i\, b_i = -2A_B\Omega(t+\Delta t) - \sum_{i=1}^{N} \Gamma_i^*, \tag{24}$$

with Γ_i^* the strength of the particle after use of the modified PSE. There are thus $M+1$ equations, with M unknowns. This overdetermined system is solved in the least-squares senses, but the constraint (24) is enforced exactly, using the technique of Lagrange multipliers.

3.4. *Vortex Sheet Diffusion*

The total flux to be emitted into the flow for the other substep of the diffusion process is given by

$$\nu \frac{\partial\omega}{\partial \mathrm{n}} = \frac{\Delta\gamma}{\Delta t}. \tag{25}$$

This flux must be emitted during a time Δt. In effect, the vortex sheet $\Delta\gamma$ must be distributed to neighbor particles by discretizing the Green's integral for the inhomogeneous Neumann problem corresponding to the diffusion equation. See Koumoutsakos *et al.* [8] for a simple scheme in 2-D (referred to hereafter as scheme K). Winckelmans (1993, private communication), Leonard *et al.* [12], and Ploumhans *et al.* [15] have proposed a more

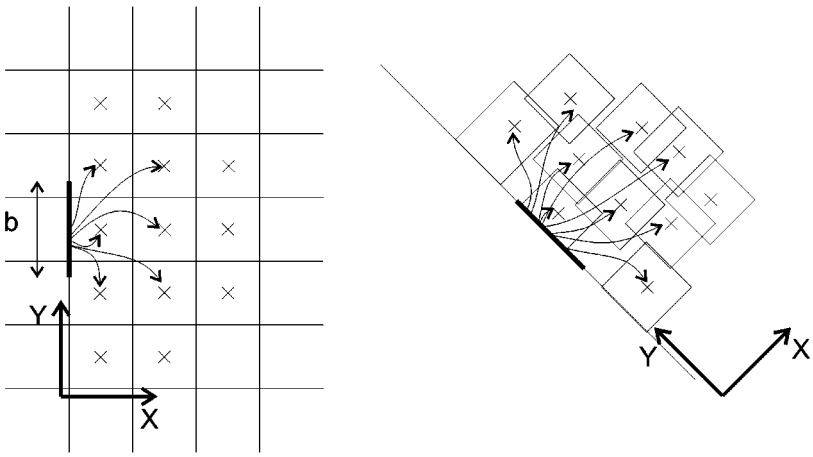

FIG. 3. Panel to particles diffusion: particles on a regular lattice aligned with the panel (left); particles with arbitrary position with respect to the panel (right).

accurate scheme (scheme W). Consider a panel of uniform strength $\Delta\gamma$ located along the y-axis, from $-b/2$ to $b/2$, and diffusing to the right (the left being the body into which the vortex sheet does not diffuse), as shown in Fig. 3. The amount of circulation, $\Delta\Gamma_i$, that must be received by the particle located at $x_i > 0$, y_i (any sign), is given by

$$\Delta\Gamma_i = \int_{x_i-h_i/2}^{x_i+h_i/2} \int_{y_i-h_i/2}^{y_i+h_i/2} \Delta\omega \, dx \, dy \tag{26}$$

with $h_i^2 = S_i$ the fluid area associated with particle i. $\Delta\omega$ stands for the change in vorticity due to the flux from the panel acting over a time Δt and is itself the result of a time integral,

$$\Delta\omega = \int_0^{\Delta t} \frac{d\omega}{dt} \, dt, \tag{27}$$

with

$$\frac{d\omega}{dt} = \frac{\Delta\gamma}{\Delta t} \frac{1}{\sqrt{\pi}} \frac{1}{\sqrt{4\nu t}} \exp\left(-\frac{x^2}{4\nu t}\right) [\mathrm{erfc}(s)]_{(y+b/2)/\sqrt{4\nu t}}^{(y-b/2)/\sqrt{4\nu t}}, \tag{28}$$

where $\mathrm{erfc}(s) = \int_s^\infty \frac{2}{\sqrt{\pi}} \exp(-v^2) \, dv$. The amount of circulation received by the particle i is

$$\Delta\Gamma_i = \int_0^{\Delta t} \frac{d\Gamma_i}{dt} \, dt, \tag{29}$$

where

$$\frac{d\Gamma_i}{dt} = \int\int \frac{d\omega}{dt} \, dx \, dy. \tag{30}$$

In scheme K, Eqs. (29) and (30) are integrated numerically using the mid-point rule:

$$\Delta\Gamma_i = S_i \Delta\gamma \frac{1}{\sqrt{2\nu\Delta t}} \frac{1}{\sqrt{\pi}} \exp\left(-\frac{x_i^2}{2\nu\Delta t}\right) [\mathrm{erfc}(s)]_{(y_i+b/2)/\sqrt{2\nu\Delta t}}^{(y_i-b/2)/\sqrt{2\nu\Delta t}}. \tag{31}$$

TABLE I
Panel to Particles Diffusion
with K Scheme

$h^2/(4\nu\Delta t)$	$(\sum_i \Delta\Gamma_i)/(b\Delta\gamma)$
1/4	1.000
1/2	0.999
1	0.986
2	0.881
4	0.592

Because the spatial integration is done numerically, this scheme is not conservative; i.e., $\Delta\gamma$ is not exactly distributed to the particles ($b\Delta\gamma \neq \sum_i \Delta\Gamma_i$). Table I contains the values of the ratio $\sum_i \Delta\Gamma_i/(b\Delta\gamma)$ for different $h^2/(4\nu\Delta t)$. It is seen that scheme K becomes less and less conservative as $h^2/(4\nu\Delta t)$ increases.

In scheme W, the integral in Eq. (30) is performed exactly, giving

$$\frac{d\Gamma_i}{dt} = \int\int \frac{d\omega}{dt}\,dx\,dy = \frac{\Delta\gamma}{\Delta t}\left([\mathrm{erfc}(s)]_{(x_i+h_i/2)/\sqrt{4\nu t}}^{(x_i-h_{i,l}/2)/\sqrt{4\nu t}}\right) \cdot \left(\sqrt{4\nu t}\frac{1}{2}\left([\mathrm{ierfc}(s)]_{((y_i+h_i/2)-h_i/2)/\sqrt{4\nu t}}^{((y_i-b/2)-h_i/2)/\sqrt{4\nu t}} - [\mathrm{ierfc}(s)]_{((y_i+h_i/2)+h_i/2)/\sqrt{4\nu t}}^{((y_i+b/2)-h_i/2)/\sqrt{4\nu t}}\right)\right), \quad (32)$$

where $\mathrm{ierfc}(s) = \int_s^\infty \mathrm{erfc}(v)\,dv = \frac{1}{\sqrt{\pi}}\exp(-s^2) - s\,\mathrm{erfc}(s)$. Notice that $h_{i,l}/2 = x_i$ if $0 \leq x_i < h_i$ and $h_{i,l}/2 = h_i/2$ otherwise. This allows for particles in the "first layer" to be closer to or further away from the y-axis than $h_i/2$ and it ensures that the scheme remains conservative in such cases. The time integral in Eq. (29) is evaluated using Gauss quadrature (3 or 4 points).

If particles are on a regular lattice aligned with the panel, scheme W is always conservative. It could thus also be used to perform under-resolved computations, where the value of $h^2/(4\nu\Delta t)$ would be very high. In practice, however, the spatial distribution of the particles is not well aligned with the vortex panel (see Fig. 3): The proposed scheme is then not exactly conservative. To enforce conservation, the following correction is made: Instead of using $\Delta\Gamma_i$ given by Eqs. (29) and (32), one uses

$$\Delta\Gamma_{i,\mathrm{conserv}} = \Delta\Gamma_i + \frac{(\Delta\Gamma_i)^2}{\sum_j (\Delta\Gamma_j)^2}\left(b\Delta\gamma - \sum_j \Delta\Gamma_j\right), \quad (33)$$

where j runs over all particles concerned by the panel $\Delta\gamma$. This scheme minimizes $\sum_i (\Delta\Gamma_i - \Delta\Gamma_{i,\mathrm{conserv}})^2/(\Delta\Gamma_i)^2$ with the constraint that $(b\Delta\gamma) - (\sum_i \Delta\Gamma_{i,\mathrm{conserv}}) = 0$.

For diffusion with the above schemes to work properly, the spatial distribution of the particles must remain fairly uniform. This is one reason particle redistribution is needed every 5 to 10 time steps. Of course, as in vortex methods without solid boundaries, it is also needed to minimize the PSE and convection errors.

Comparison of schemes K and W. Schemes K and W (this one used together with Eq. (33)) are now compared for the first time steps of the simulation of an impulsively started circular cylinder, at $\mathrm{Re} = U_\infty D/\nu = 550$. The particles are initially set on a lattice

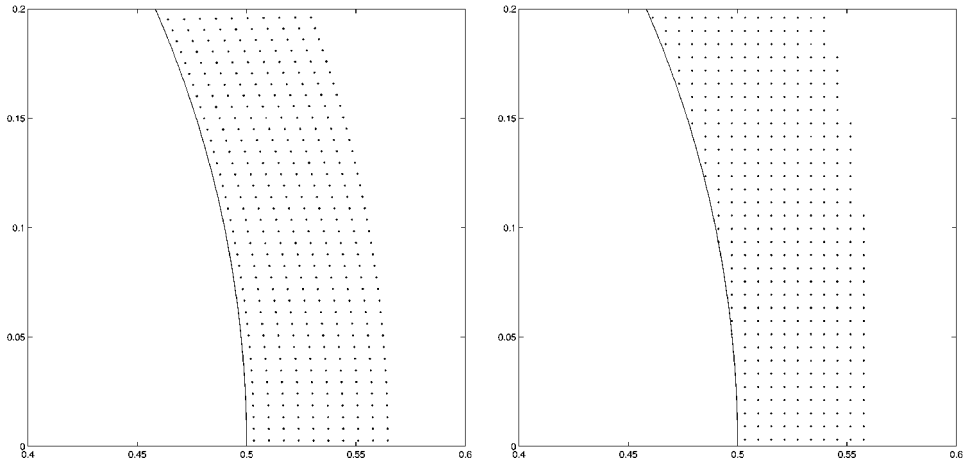

FIG. 4. The KL redistribution technique (left), and the general one (right).

that follows the boundary (Fig. 4), and $h^2/(4\nu\Delta t) = 1/2$. The other relevant parameters of this simulation are given in Section 4.1. Figure 5 compares the linear impulse, $I_x = \int_\Omega y\,\omega\,d\Omega = \sum_p y_p\Gamma_p$, obtained with the two schemes with an analytical solution valid for short times [1]. It is seen that, for this flow and with particles following the boundary, both schemes give accurate results, with scheme W performing slightly better.

3.5. *Particle Redistribution*

In accurate particle methods for direct numerical simulation (DNS) of viscous flows, one needs to maintain the condition that particle cores overlap. This calls for a particle redistribution scheme. It consists in replacing the distorted set of vortex particles by a new set where the particles are, again, located on an $h \times h$ lattice. If σ is not the same for each particle, the redistribution is performed in a mapped domain (see Section 3.6) in

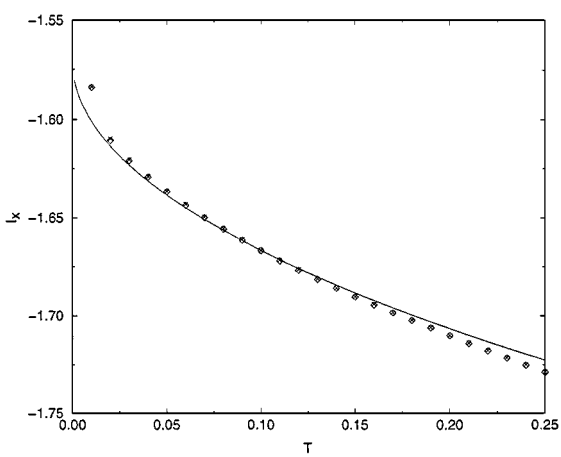

FIG. 5. I_x comparison for short times for an impulsively started circular cylinder, at Re = 550: analytical (solid line), W scheme (◇), K scheme (×).

which particles are located on a 1×1 mapped lattice after redistribution. Consider first the normalized 1-D problem with unit spacing. In the $\Lambda_3(x)$ scheme (that conserves up to order $p = 3$ of the vorticity distribution; recall that $p = 0$ is the circulation, $p = 1$ is the linear impulse, and $p = 2$ is the angular impulse), an old particle located at $-1/2 \le x \le 1/2$ gives

$$\begin{aligned}
&(3-2x)(4x^2-1)/48 && \text{to the new particle located at } -3/2\\
&(1-2x)(9-4x^2)/16 && \text{to the new particle located at } -1/2\\
&(1+2x)(9-4x^2)/16 && \text{to the new particle located at } 1/2\\
&(3+2x)(4x^2-1)/48 && \text{to the new particle located at } 3/2.
\end{aligned} \tag{34}$$

If a wall is present, the redistribution of particles close to the wall must be modified, because particles are not allowed inside the body. This is achieved by using decentered Λ'_p schemes. Two such schemes are detailed here, considering that an old particle is located at $-\frac{1}{2} \le x \le \frac{1}{2}$ and that the wall is at $x = -\frac{1}{2}$ for the Λ'_2 scheme and at $x = -1$ for the Λ'_3 scheme:

$$\Lambda'_2(x) \text{ gives } \begin{cases}
(x-2)(x-1)/2 & \text{to the new particle located at } 0\\
x(2-x) & \text{to the new particle located at } 1\\
x(x-1)/2 & \text{to the new particle located at } 2
\end{cases} \tag{35}$$

$$\Lambda'_3(x) \text{ gives } \begin{cases}
(1-2x)(2x-5)(2x-3)/48 & \text{to the new particle located at } -1/2\\
(2x-5)(2x-3)(1+2x)/16 & \text{to the new particle located at } 1/2\\
(1-2x)(2x-5)(1+2x)/16 & \text{to the new particle located at } 3/2\\
(1-2x)(3-2x)(1+2x)/48 & \text{to the new particle located at } 5/2.
\end{cases} \tag{36}$$

In the present approach, a Λ_3 scheme is used for particles located more than $3/2$ from the wall, a Λ'_3 scheme for particles with distance between $1/2$ and $3/2$, and a Λ'_2 scheme for particles less than $1/2$ from the wall.

In 2-D, the problem of deciding which scheme to use near the boundaries is more involved because, in general, the boundary crosses the redistribution lattice in an arbitrary way. Two steps are used. First, an old particle is redistributed in the x-direction and temporary particles are created. A Λ_3 scheme is used if it is possible (that is, if it doesn't introduce particles inside the body); if not, a Λ'_3 scheme is used and if it still leads to the creation of particles inside the body, a Λ'_2 scheme is chosen. This redistribution in the x-direction has thus created four (Λ_3 or Λ'_3) or three (Λ'_2) temporary particles. Each temporary particle is then redistributed in the y-direction using, in order of preference, a Λ_3, Λ'_3, or Λ'_2 scheme. Note that the scheme used in the y-direction is not necessarily the same for each temporary particle. A penalty p_i is given to each new particle, with

$$p_i = \begin{cases}
0 & \text{if only centered schemes were used}\\
1 & \text{if a } \Lambda'_p \text{ scheme was used for the } x\text{- or the } y\text{-direction}\\
2 & \text{if } \Lambda'_p \text{ schemes were used for both the } x\text{- and } y\text{-directions.}
\end{cases}$$

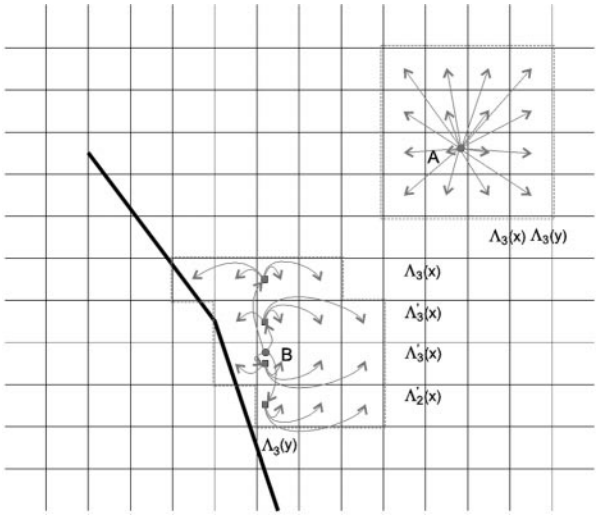

FIG. 6. 2-D redistribution schemes: Λ_3 for point A; $\Lambda_3\Lambda_3'\Lambda_2'$ for point B.

This leads to the creation of N_{np} new particles. A global penalty is then computed:

$$P_{XY} = \frac{\sum_{i=1}^{N_{\text{np}}} p_i}{N_{\text{np}}}. \tag{37}$$

In a second step, the global penalty P_{YX}, obtained when doing the redistribution first in the y-direction and then in the x-direction, is computed. In the end, the order of redistribution chosen is the one that leads to the lowest global penalty. If $P_{XY} = P_{YX}$, an average of the two schemes is used.

Figure 6 gives an example of the $\Lambda_3\Lambda_3'\Lambda_2'$ redistribution scheme. Particle A is far from the walls, so a Λ_3 scheme is used in both directions. Particle B is close enough to the wall that decentered schemes have to be used: One has $P_{XY} = \frac{20}{16}$ and $P_{YX} = \frac{11}{15}$, so the redistribution proceeds first in the y-direction and then in the x-direction.

The surface, $S_i = h_i^2$, of each particle in the new set is determined by the mapping (see Section 3.6). The smoothing parameter is taken as $\sigma_i = \beta h_i$ with β the core overlapping parameter (typically, $\beta = 1$ for the Gaussian as defined in Eq. (8)). For particles close to the body, the surface is "corrected" to take into account the fact that part of the area S_i associated to particle i is "inside" the body.

3.6. *Redistribution with Mapping of the Physical Domain*

In external flows, the vorticity is located in the boundary layer and in the wake, with the magnitude of the vorticity decreasing as one goes downstream. Thus it would be more efficient to have high resolution near the body and coarser resolution in the far wake. To achieve this, the physical domain, with spatially varying resolution, is mapped onto a regular indicial lattice (i, j) (Cottet *et al.* [3], Lemine [11], Cottet and Koumoutsakos [4]). Different mappings can be considered. One example is the exponential mapping given by

$$\begin{aligned} x &= x_0 + r(i)\ \cos\theta(j) \\ y &= y_0 + r(i)\ \sin\theta(j) \end{aligned} \tag{38}$$

with $\theta(j) = \frac{2\pi}{m} j$, $0 \le j \le m$, and $r(i) = R_0 f(i)$, $i \ge 0$. The function $f(i)$ is chosen such that all cells are "almost" square:

$$r\, d\theta = dr \quad \text{when} \quad di = dj. \tag{39}$$

This leads to the following expression for $f(i)$:

$$f(i) = \exp\left(\frac{2\pi}{m} i\right). \tag{40}$$

After each redistribution, new particles in the mapped domain have position $(i + 1/2, j + 1/2)$ and the corresponding positions obtained from Eqs. (38) and (40) in the physical domain. The fluid area associated with the particle is

$$\begin{aligned} S = \int\int r\, d\theta\, dr &= \int_i^{i+1} \int_j^{j+1} r\, \frac{d\theta}{dj}\, dj\, \frac{dr}{di}\, di \\ &= \frac{\pi}{m} R_0^2 \left(\exp\left(\frac{4\pi}{m}(i+1)\right) - \exp\left(\frac{4\pi}{m} i\right)\right) \qquad (41) \\ &= \frac{\sinh(2\pi/m)}{(2\pi/m)} \left(\left(\frac{2\pi}{m}\, R_0\right) \cdot \exp\left(\frac{2\pi}{m}(i+1/2)\right)\right)^2. \qquad (42) \end{aligned}$$

Notice that, for small $2\pi/m$, this further reduces to

$$S = h^2 \simeq \left(\left(\frac{2\pi}{m}\, R_0\right) \cdot \exp\left(\frac{2\pi}{m}(i+1/2)\right)\right)^2 \tag{43}$$

and thus

$$h \simeq \left(\frac{2\pi}{m}\, R_0\right) \cdot \exp\left(\frac{2\pi}{m}(i+1/2)\right). \tag{44}$$

The smoothing parameter, σ, associated to the particle is given by

$$\sigma(i) = \beta h, \tag{45}$$

where β is the core overlapping parameter (which is the same for all particles). For the Gaussian, $\beta = 1$ is used.

The use of this mapping produces a σ that varies smoothly in space (so that Eq. (20) can be used safely, preserving second-order accuracy of the PSE; see Appendixes A and B).

3.7. *Quality Criterion for a Vortex Simulation*

To gauge the quality of a numerical simulation, one has to consider the "mesh" Reynolds number. In vortex methods, it is natural to use the "mesh" Reynolds number based on vorticity:

$$\mathrm{Re}_h = \frac{|\omega|\, h^2}{\nu}. \tag{46}$$

A well-resolved simulation is one such that

$$\mathrm{Re}_h = \mathcal{O}(1), \tag{47}$$

as this ensures that the relevant viscous scales present in the flow are resolved.

To accurately resolve the diffusion phenomena, it is required to have

$$\frac{\nu \Delta t}{h^2} = \mathcal{O}(1). \tag{48}$$

Multiplying Eq. (47) by Eq. (48), one finds that

$$|\omega| \Delta t = \mathcal{O}(1). \tag{49}$$

This basically ensures that particles do not rotate too much with respect to each other (recall that $\omega/2$ is the rotation of a fluid element).

The PSE is also subjected to a stability constraint that requires that

$$\frac{\nu \Delta t}{\sigma^2} < \phi, \tag{50}$$

where ϕ depends on the smoothing function, the core overlapping parameter, β, and the scheme used for the time integration.

It is possible to carry out an analysis of the stability of the PSE and to find a lower bound on ϕ (hereafter referred to as ϕ^*). For the Gaussian, with $\beta = 1$, one finds:

- for the Euler explicit scheme, $\phi^* = 0.595$,
- for the Adams–Bashforth 2 scheme, $\phi^* = 0.297$.

4. FLOW PAST AN IMPULSIVELY STARTED CYLINDER AT UNIFORM RESOLUTION

In this section, the general method, with uniform spatial resolution h, is tested on the flow past an impulsively started cylinder. This flow is interesting because: (1) it is a benchmark for bluff body flows; (2) there exists an analytical solution valid for short times (Bar-Lev and Yang [1]); and (3) this flow has been extensively studied by Koumoutsakos and Leonard [9], using a vortex method, but with a redistribution technique specifically designed for the circle, who showed that the vortex method compared very well with other numerical techniques on that flow.

Figure 4 shows the difference between the KL-like approach and the general method. In the KL-like method, the particles are initially (and also after each redistribution) located in a way that "follows" the boundary, but each particle still has an area of h^2 associated with it. This is clearly the best one can do to obtain accurate results for the flow past the cylinder. However, it cannot be extended to general geometries.

A redistribution technique similar to what was used in KL has been implemented, in order to have a "KL-like reference" solution for long times. Redistribution is done with a Λ_3 scheme in the θ-direction and with, in order of preference, a Λ_3, Λ_3', or Λ_2' scheme in the r-direction. Notice that, in all that follows, "KL-like" is used to refer to a "Koumoutsakos–Leonard-like" method, even though it was here improved using (1) the modified PSE (Section 3.2), and (2) the more accurate wall vorticity flux (Sections 3.3 and 3.4).

Two sets of simulations were carried out: the first one corresponds to a Reynolds number $\mathrm{Re} = U_\infty D/\nu = 550$, and the second one to $\mathrm{Re} = 3000$. Also, several variations of the method presented in the previous sections were tested:

- the use of random "vibrations": at each redistribution, the center of the "redistribution lattice" is chosen randomly in $[-h/2; h/2] \times [-h/2; h/2]$;
- the use of a "halo" around the body: at each redistribution, when particles are redistributed on a regular $h \times h$ lattice, a minimal distance, d_{halo}, between a new particle and the body surface is required;
- the combination of the two methods above.

Hereafter, the general method and its three variations will be referred to as G, G + V, G + H, and G + H + V, respectively.

Different comparisons are made as a function of $T = tU_\infty/D$: the x-component of momentum, $I_x = \int_\Omega y\omega\, d\Omega = \sum_p y_p \Gamma_p$, and the drag coefficient, $C_\mathrm{D} = F_x/\frac{1}{2}\rho U_\infty^2 D$ with $F_x = -\rho\, dI_x/dt$, where $dI_x/dt \approx (I_x(t + \Delta t) - I_x(t - \Delta t))/(2\Delta t)$ (in order to avoid spurious noise due to redistributions, the I_x curve is filtered using a 5-point moving average before the numerical differenciation). It is also of interest to compare the production of circulation from the upper part of the cylinder, $d\Gamma_{\mathrm{up}}/dt = \nu R \int_0^\pi \frac{\partial \omega}{\partial r}\, d\theta$. This can be easily obtained from the computed panel values only, Eq. (25), since, in our method, the use of PSE images guarantees a zero vorticity flux during the PSE step. In some cases, the production of circulation has revealed itself as a better diagnostic than the drag coefficient for the comparison of the different schemes. Isocontours of vorticity are also compared. Finally, we compare the values of the panels' strength. This is a very tough comparison, as it concerns the vorticity flux at the boundary. The general method exhibits a high-frequency noise in the vorticity flux, and the comparison is thus also carried out in the Fourier domain.

4.1. *Re = 550*

The parameters of the simulation are $\Delta T = 0.01$ and $h/D = 6.03 \times 10^{-3}$. Gaussian particles are used, with $\beta = \sigma/h = 1$. Redistribution is done every five time steps. If a new particle has $|\Gamma_i| < 0.001|\Gamma_i|_{\max}$, it is deleted (in order to avoid too high a growth rate for the number of particles), and the loss of circulation, Γ_i, is redistributed equally among the remaining particles. The presence of 10 layers of particles around the body is also enforced after each redistribution. When a "halo" is used, $d_{\mathrm{halo}} = b/4$, with b the length of a panel. There are $M = 592$ panels. Thus $b/D = \pi/592 = 5.31 \times 10^{-3}$. In the KL-like method, this corresponds, for the first layer of particles after redistribution, to one particle in front of each panel. The area associated with these particles is then $S = 3.63 \times 10^{-5}$, the square root of which is equal to $h = \sqrt{S} = 6.03 \times 10^{-3}$. Equation (29) is integrated with four Gauss points. The integration scheme for convection is a second-order Adams–Bashforth (second-order Runge–Kutta for the first step and after each redistribution); for PSE diffusion, a first-order Euler explicit scheme is used. A fast tree code is used, with multipole expansions of third order. The mean error estimate (on the norm of the velocity) is $\sim 3 \times 10^{-3} U_\infty$, the number of particles goes from ~5000 to ~70,000 during the course of the simulation, and the total run time is ~3 h on a DEC alpha running at 433 Mhz.

Figure 7 shows a comparison between the analytical expression of I_x for short times and I_x computed with the different methods. In this figure, the KL-like method gives the results

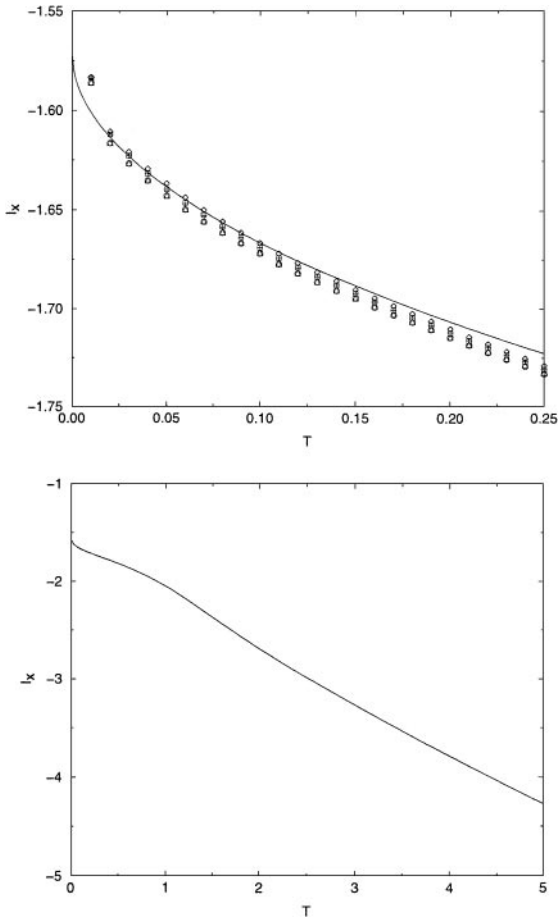

FIG. 7. I_x comparison for an impulsively started circular cylinder, at Re = 550. Short time (top): analytical (solid line), KL-like (◇), G (+), G + V (□), G + H (○), G + H + V (△). Long time (bottom): KL-like (solid line), G + V (dashed line).

closest to the analytical prediction; the methods G and G + V give almost identical results, which are not quite as good as those obtained using the KL-like approach. This, of course, is to be expected, as the same resolution was used for a body-fitted method versus a general, non-body-fitted method. The methods G + H and G + H + V also give almost identical results, but these are not as good as those of the three other methods. When I_x is compared for longer times, all five methods give results that cannot be distinguished (thus, for clarity, only the results from the KL and G + V methods have been shown in Fig. 7).

A comparison of the drag coefficient, C_D, is shown in Fig. 8. Since all five approaches give almost identical results, not all results are shown in Fig. 8. It is interesting to zoom in on the parts of the graph corresponding to local extrema of the drag coefficients. The graphs of Fig. 9 show that the methods G and G + V give results closer to those of the KL-like method. Also, the G + V and G + H + V methods exhibit somewhat higher noise levels.

Figure 10 illustrates the fact that half the total production of circulation, $d\Gamma_{up}/dt$, allows a better distinction between the different methods than the drag coefficient. It is calculated directly by summing the strengths of half the panels. To smooth out high-frequency noise

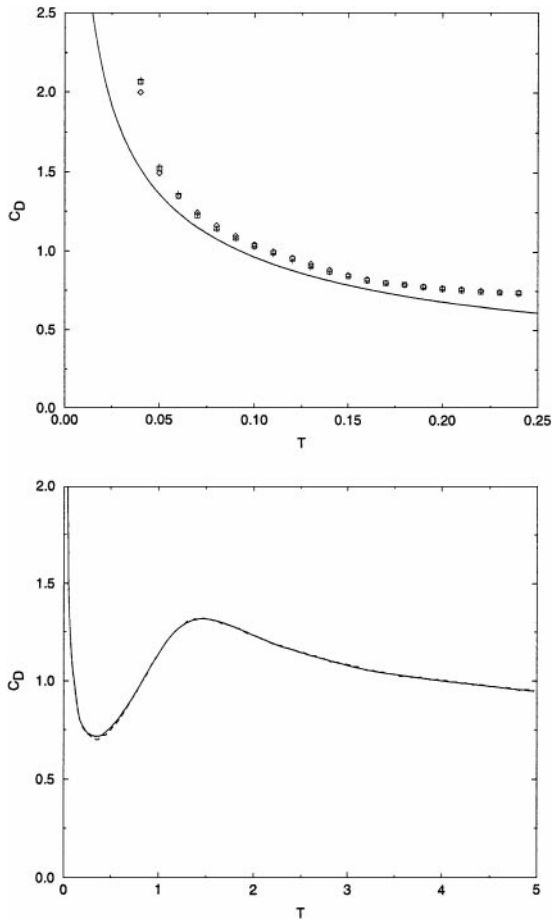

FIG. 8. C_D comparison for an impulsively started circular cylinder, at Re $= 550$. Short time (top): analytical (solid line), KL-like ($\diamond$), G ($+$), G + V ($\square$). Long time (bottom): KL-like (solid line), G + V (dashed line).

due to redistribution, this curve is filtered using a five-point moving average. Figure 11 focuses on the parts of Fig. 10 where the methods differ most. From Figs. 10 and 11, it is seen that the G + V method is the one that gives results closest to those of the KL-like method.

Figure 12 shows a comparison of iso contours of vorticity for the KL-like and G + V approaches. The agreement between these techniques is very good, although the minimum and maximum value of ω are slightly different (because they correspond to particles very close to the wall). Also, a small asymmetry is present in the minimum and maximum values of the vorticity for the methods using small random "vibrations" of the redistribution lattice (G + V and G + H + V). Short-wavelength oscillations in the low-value iso contours are present at positions where the contours come very close to the region with no particles.

Figure 13 compares the 16 first modes of the vortex sheet's strength, $\Delta\gamma$, at $T = 1$ and $T = 5$ for the KL-like and G + V methods. It also shows the "filtered" strength of the vortex sheet (obtained through an inverse Fourier transform of the 16 first modes) at the same times. The agreement between the two methods is seen to be quite good; the small differences are more noticeable at the local extrema.

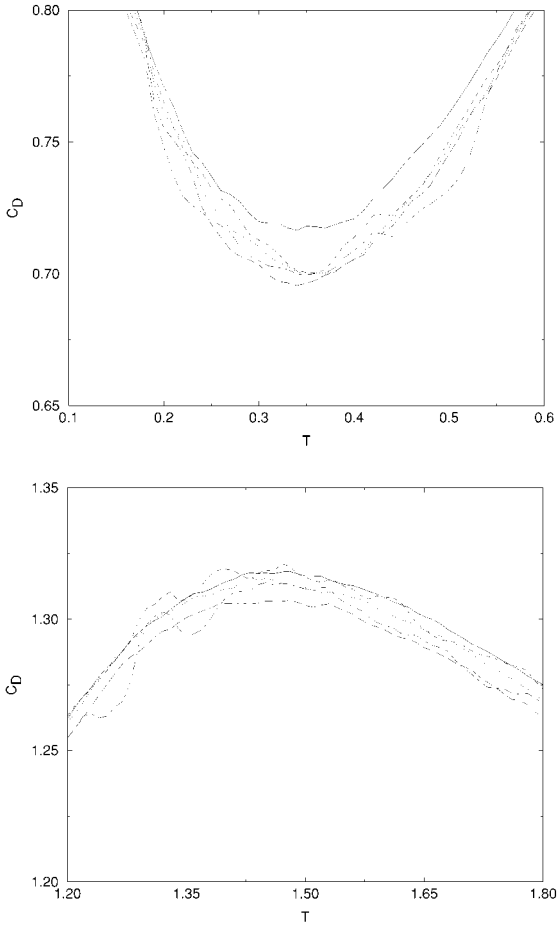

FIG. 9. C_D comparison for an impulsively started circular cylinder, at Re = 550: KL-like (solid line), G (dotted line), G + V (dashed line), G + H (dot-dashed line), G + H + V (long dashed line).

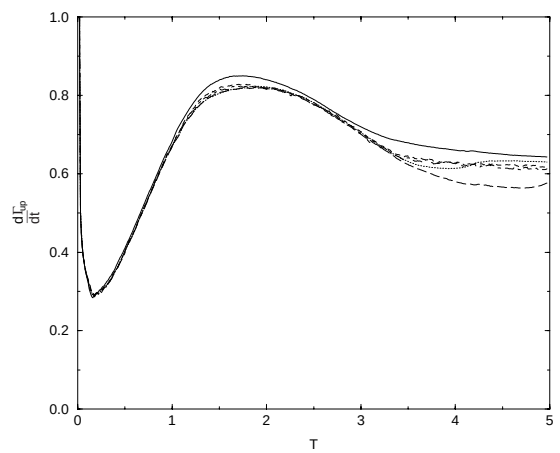

FIG. 10. $d\Gamma_{up}/dt$ comparison for an impulsively started circular cylinder, at Re = 550: KL-like (solid line), G (dotted line), G + V (dashed line), G + H (dot-dashed line), G + H + V (long dashed line).

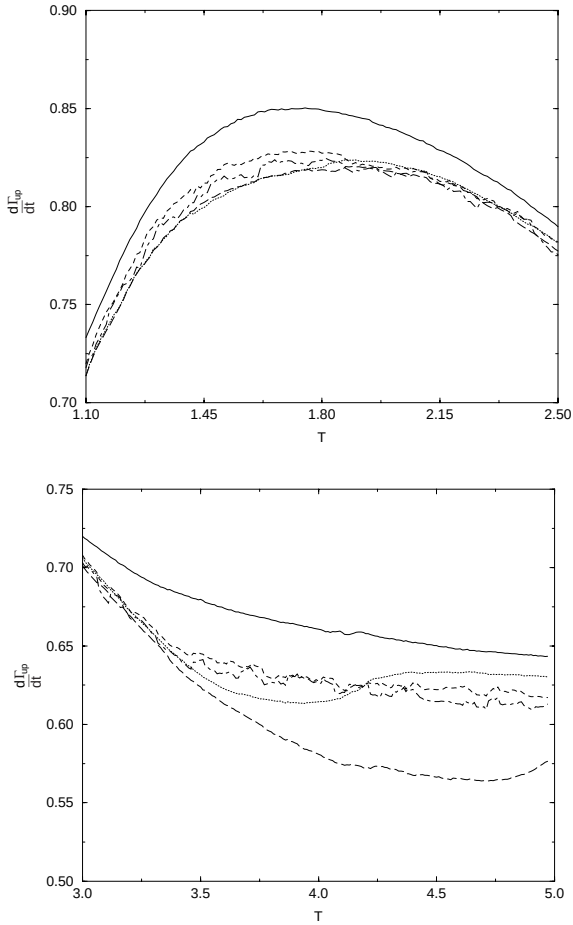

FIG. 11. $d\Gamma_{\text{up}}/dt$ comparison for an impulsively started circular cylinder, at Re = 550: KL-like (solid line), G (dotted line), G + V (dashed line), G + H (dot-dashed line), G + H + V (long dashed line).

As mentioned above, our general method cannot, at the same resolution (h, b), be expected to be as good as the body-fitted method. A convergence analysis of the G + V method is thus carried out. Two simulations of the same flow are made: one at $h/D = 6.03 \times 10^{-3}$, $\Delta T = 0.01$, and one at $h/D = 3.015 \times 10^{-3}$, $\Delta T = 0.025$. Thus, both have the same $\nu \Delta t/h^2 = 1/2$. Figure 14 shows that the G + V method indeed converges well: The values of I_x and C_D obtained with the smaller h/D are remarkably close to the analytical values. The other schemes were also tested and shown to converge.

4.2. *Re = 3000*

The parameters of the simulations are $\Delta T = 0.005$ and $h/D = 1.87 \times 10^{-3}$. There are 1944 panels, the number of particles goes from ∼20,000 to ∼500,000, and the total run time is approximately 60 h on a DEC alpha running at 533 Mhz.

The short-time comparison of I_x indicates, once again, that, at the same resolution (h, b), the body-fitted KL-like method works slightly better and that the G and G + V methods work better than the G + H and G + H + V ones. For longer times, all four general methods

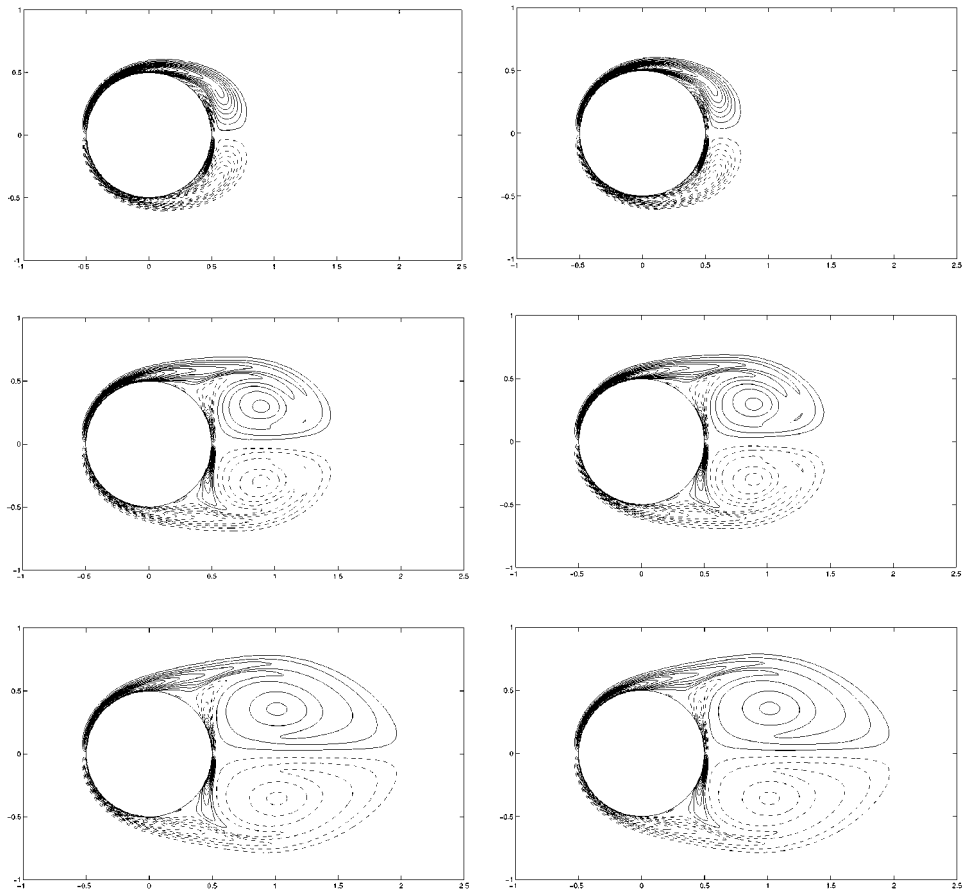

FIG. 12. Iso contours of vorticity for $T = 1$, 3, and 5 for an impulsively started circular cylinder, at Re $= 550$: KL-like (left), G + V (right). Levels are by steps of 2 (zero level is skipped).

work equally well, so only the results from the G + V method are shown in Fig. 15, along with those obtained using the KL-like method.

Figure 16 illustrates the results for the drag coefficient, C_D. Once again, the results of all four general methods are very similar. However, for Re $= 3000$, there are slight but noticeable differences in the long-time C_D computed with the KL-like and G + V methods.

Half the total production of circulation (Fig. 17) does not allow us to distinguish the different method as easily as for the Re $= 550$ case. There are, however, small differences that seem to indicate that the G + V method works best, but it is not as clear as for the Re $= 550$ case. The G and G + H methods give results very similar and are not shown.

Figure 18 shows a comparison of the iso contours of vorticity for the KL-like and G + V methods. Although the agreement is very good, there are some differences between the two methods, and they increase with time.

Figure 19 compares the 48 first modes of the vortex sheet's strength, $\Delta\gamma$, at $T = 1$ and $T = 5$ for the KL-like and G + V methods. It also shows the "filtered" strength of the vortex sheet (obtained through an inverse Fourier transform of the 48 first coefficients) at the same times. The agreement between the two methods is very good; the small differences are more noticeable at the local extrema.

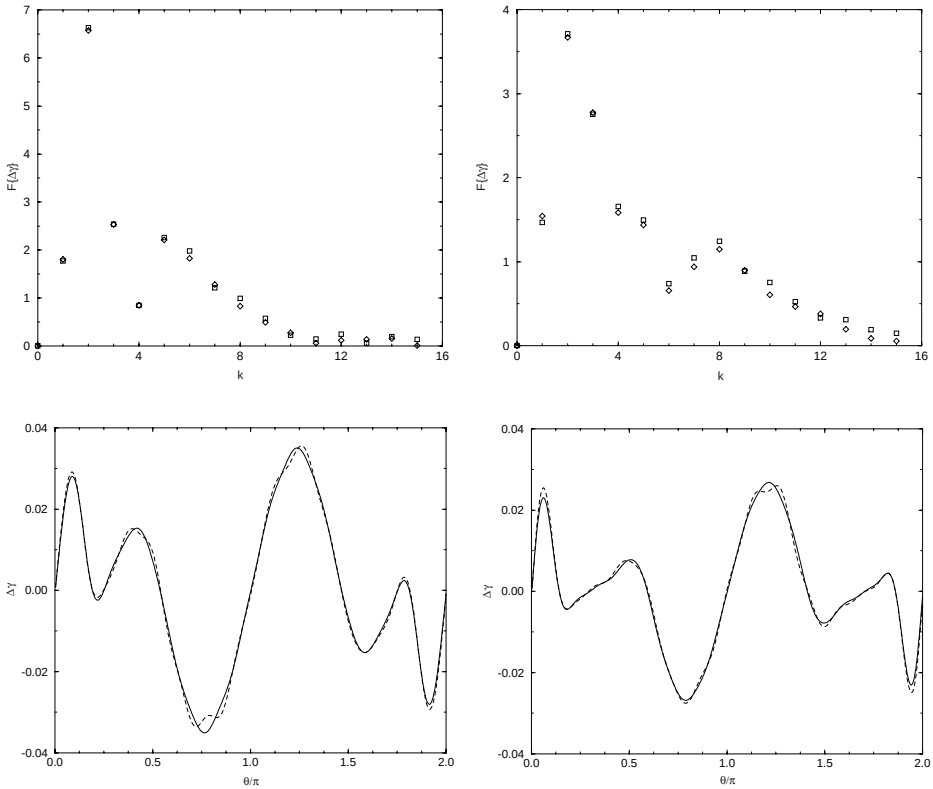

FIG. 13. Comparison of the vortex sheet's strength for an impulsively started circular cylinder, at Re $= 550$: 16 first Fourier coefficients at $T = 1$ (top left) and $T = 5$ (top right), KL-like ($\diamond$) and G + V ($\square$); filtered strength of the vortex sheet as a function of θ/π at $T = 1$ (top left) and $T = 5$ (top right): KL-like (solid line) and G + V (dashed line).

5. FLOW PAST AN IMPULSIVELY STARTED CYLINDER AT NONUNIFORM RESOLUTION

The aim of this section is to validate the "adaptive" part of the vortex method, that is, the fact that particles having, at each redistribution, a fluid area $S = h^2$ and a smoothing parameter $\sigma = \beta h$, varying slowly in space, allow one to perform an accurate simulation at a reduced computational cost. To concentrate on only that part of the validation study, one has to consider the flow past a circular cylinder together with the exponential mapping, with the center of the mapping being located at the center of the cylinder. This is thus a KL-like method but with nonuniform resolution.

Two sets of simulations have been performed: Re $= 550$ and Re $= 3000$. For each set, the linear impulse, I_x, the drag coefficient, C_D, the half total production of circulation, $d\Gamma_{up}/dt$, and the iso contours are compared with the results from the KL-like method with uniform resolution.

5.1. *Re = 550*

The parameter m for the exponential mapping is $m = 592$, that is, the number of panels. All the other parameters are the same as those used in Section 4.1.

Figures 20 and 21 show that the nonuniform method gives results very similar to those obtained with uniform resolution. The evolution of the number of particles in the two

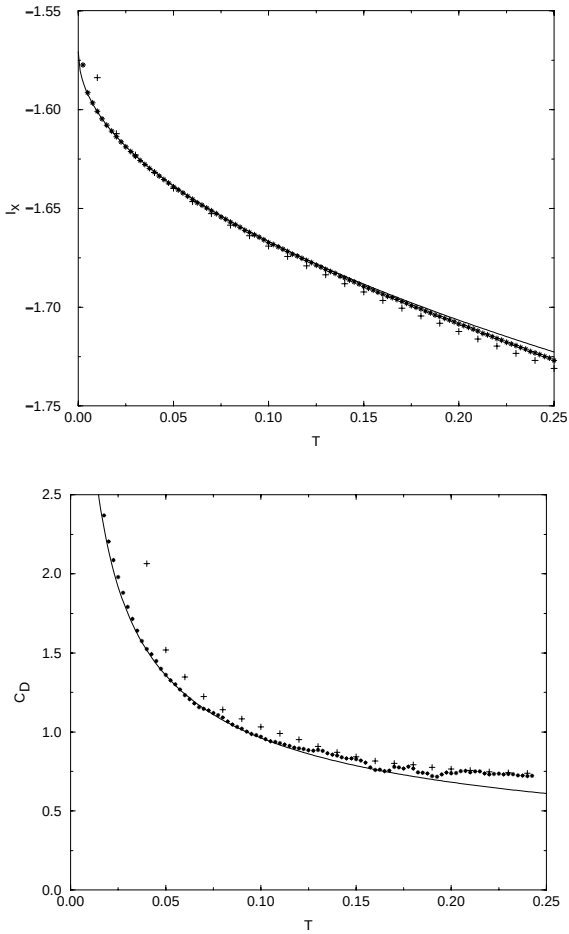

FIG. 14. Convergence of I_x for the G + V approach (top) and of C_D (bottom) for an impulsively started circular cylinder, at Re = 550: analytical (solid line), $h/D = 6.03 \times 10^{-3}$, $\Delta T = 0.01$ (+); $h/D = 3.015 \times 10^{-3}$, $\Delta T = 0.025$ (∗).

methods is shown in Fig. 28. For longer times, the I_x and C_D curves, although very close, show some differences. In fact, the uniform-resolution G + V method (Section 4.1) gives slightly better long-time results than the nonuniform KL-like method. This is due to the decreasing resolution as one goes downstream. The half total production of circulation is shown (Fig. 22) to give very similar results whether one uses the uniform or the nonuniform KL-like method. In this regard, the results from the nonuniform KL-like method are slightly better than those of the uniform G + V method. This is due to the way particles are arranged near the body. In the KL-like methods, particles "follow" the body. The particles from the "first layer" are at a distance $h/2$ from the body surface, and the vortex sheet generated at the surface, $\Delta\gamma$, is a smooth function. In the general redistribution methods, however, particles may come very close to the wall. This leads to a $\Delta\gamma$ that is noisier. Since $d\Gamma_{\text{up}}/dt$ is directly computed from $\Delta\gamma$ (and is thus a "local" rather than "global" diagnostic), it explains why the KL-like methods, even with a coarser resolution downstream, give better results for the half total production of circulation. Figure 23 shows that the iso contours of the uniform and nonuniform KL-like methods compare very well.

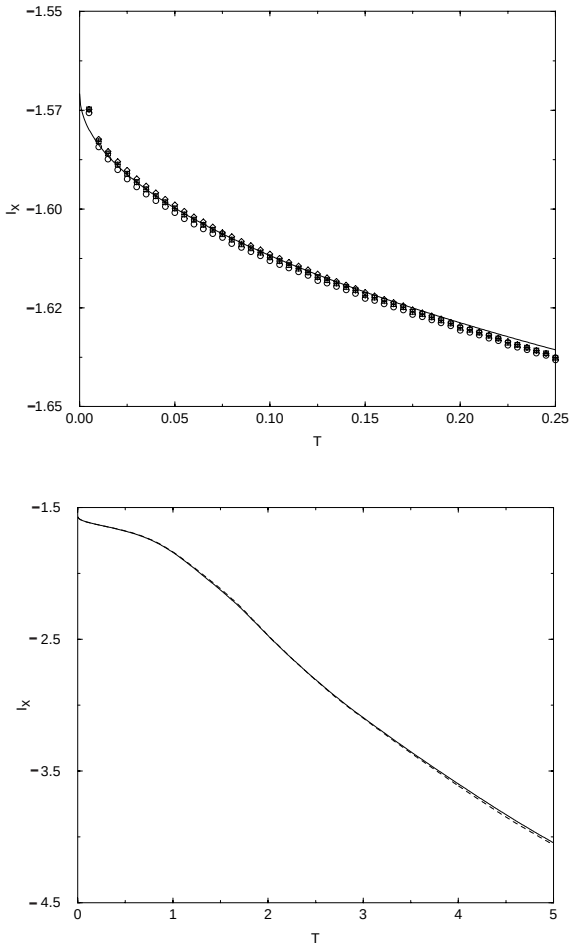

FIG. 15. I_x comparison for an impulsively started circular cylinder, at Re $= 3000$. Short time (top): analytical (solid line), KL-like ($\diamond$), G $(+)$, G + V ($\square$), G + H ($\bigcirc$), G + H + V ($\triangle$). Long time (bottom): KL-like (solid line), G + V (dashed line).

5.2. *Re = 3000*

This time, the parameter m equal to the number of panels is $m = 1944$. All other parameters are the same as those used in Section 4.2.

Figures 24, 25, 26, and 27 illustrate the performances of the nonuniform method at Re $= 3000$. The conclusions are similar to those presented in Section 5.1. The main point of interest of the nonuniform method—its use of much fewer particles for a similar accuracy in the vicinity of the body—is illustrated in Fig. 28.

6. FLOW PAST AN IMPULSIVELY STARTED SQUARE AT NONUNIFORM RESOLUTION

In this section, the flow past an impulsively started square at an angle of attack, $\alpha = 15^\circ$, is computed, taking advantages of both the general redistribution technique, which allows one to redistribute particles near bodies of general geometry, and the nonuniform scheme.

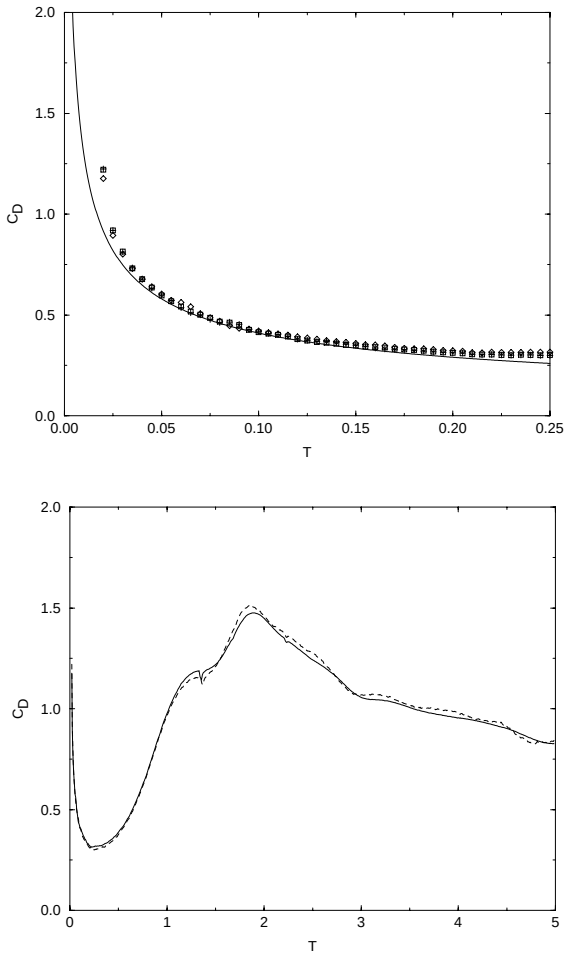

FIG. 16. C_{D} comparison for an impulsively started circular cylinder, at Re $=$ 3000. Short time (top): analytical (solid line), KL-like ($\diamond$), G ($+$), G $+$ V ($\square$). Long time (bottom): KL-like (solid line), G $+$ V (dashed line).

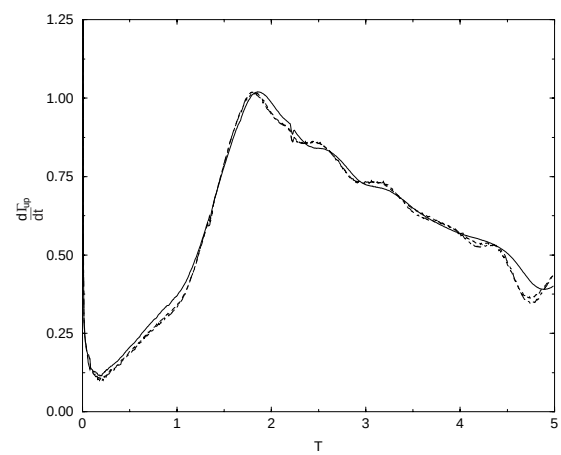

FIG. 17. $d\Gamma_{\mathrm{up}}/dt$ comparison for an impulsively started circular cylinder, at Re $=$ 3000: KL-like (solid line), G $+$ V (dashed line), G $+$ H $+$ V (long dashed line).

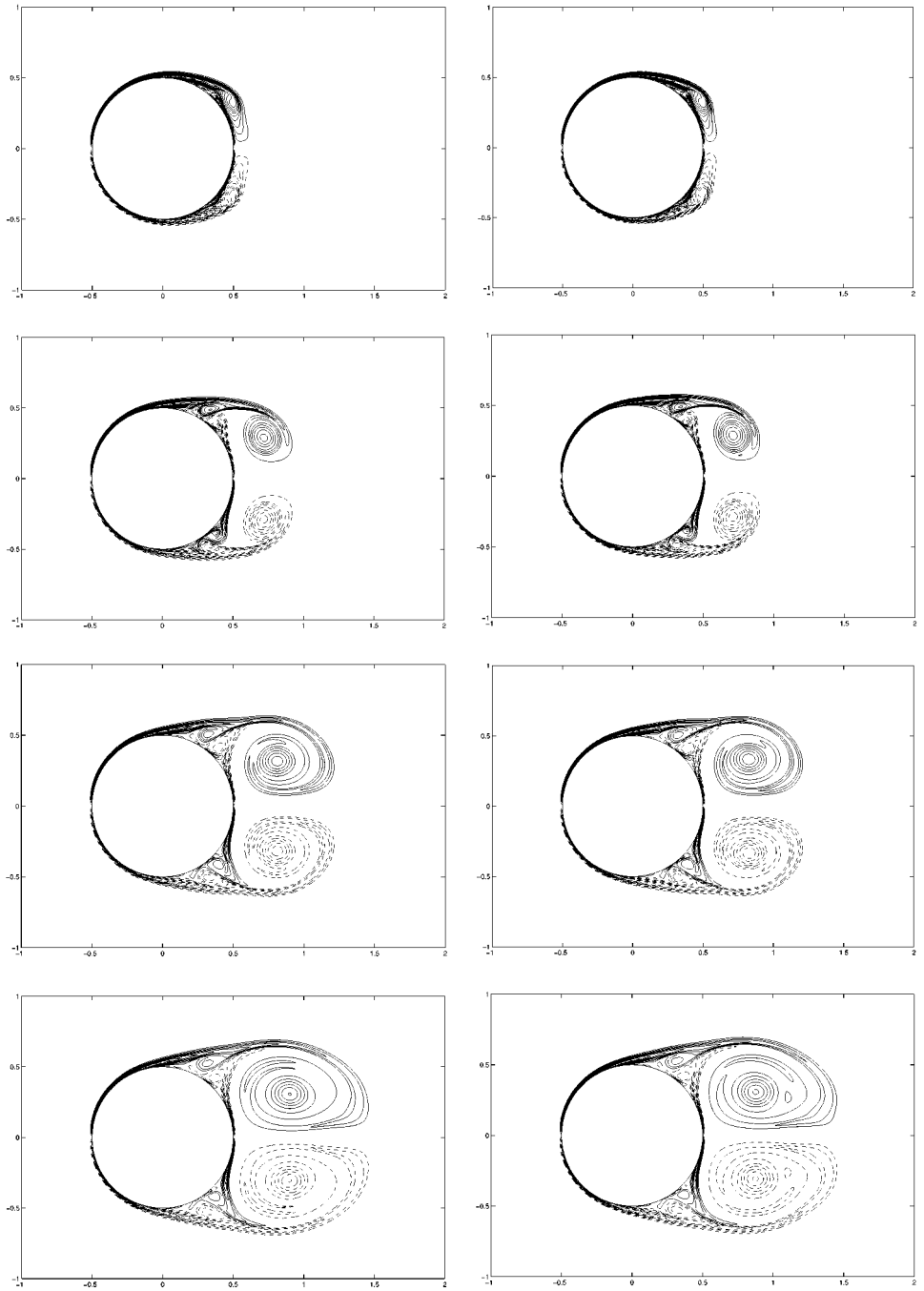

FIG. 18. Iso contours of vorticity for $T = 1, 2, 3$, and 4 for an impulsively started circular cylinder, at Re = 3000: KL-like (left), G + V (right). Levels are by steps of 4 (zero level is skipped).

The combination of these two powerful techniques makes it possible to compute this flow up to times that a uniform-resolution technique could not reach.

Two runs of this flow were performed. Both correspond to a Reynolds number $\mathrm{Re} = U_\infty c/\nu = 100$, where c is the length of a side of the square, but the parameters x_0, y_0, and

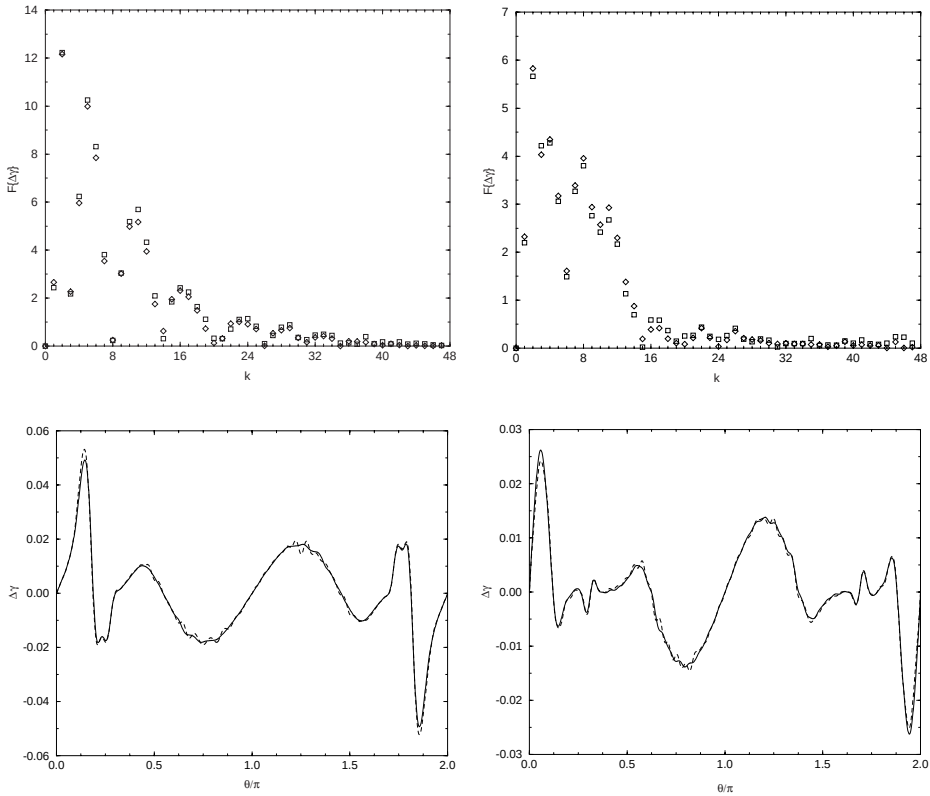

FIG. 19. Comparison of the vortex sheet's strength for an impulsively started circular cylinder, at Re $= 3000$: 48 first Fourier coefficients at $T = 1$ (top left) and $T = 5$ (top right), KL-like ($\diamond$) and G + V ($\square$); filtered strength of the vortex sheet as a function of θ/π at $T = 1$ (top left) and $T = 5$ (top right): KL-like (solid line) and G + V (dashed line).

m of the mapping are different. These three parameters enable one to control the variation of the resolution in space. Indeed, the typical distance between particles, h, varies as $h = \frac{2\pi}{m} r$, where $r^2 = (x - x_0)^2 + (y - y_0)^2$. The first run, hereafter referred to as S_1, has $m = 300$ and $(x_0, y_0) = (0, 0)$. For the second run, S_2, the values of these parameters are $m = 850$ and $(x_0, y_0) = (-2.5, -0.67)$. Both runs have $R_0 = 0.5$. These two mappings lead to the same value of h at the lower-left corner of the square, $(-0.5, -0.5)$. Figure 29 illustrates the two mappings corresponding to S_1 and S_2, where, for clarity of the figure, the values of m have been divided by 2. Figure 30 shows the position of particles at $T = 0$ and the cells of the mapping (this time with the true values of m). The other parameters, common to S_1 and S_2, are $\Delta T = 0.01$ and the use of Gaussian particles with $\beta = 1$. Each side of the square is divided into 72 panels. However, the corners of the square have to be "rounded" to avoid numerical problems. This is done by replacing the two panels at a corner by four smaller panels whose ends are on a circle of radius equal to the length of a panel.

For the panels to be able to diffuse their vorticity correctly it is essential to have enough particles around the body during the course of the simulation. The presence of a layer of n_l particles is enforced after each redistribution and also before the first time step in the following way: For each position (i, j) of the redistribution lattice in the mapped domain, a square centered at (i, j) and of side of length $2n_l + 1$ is considered. If any position

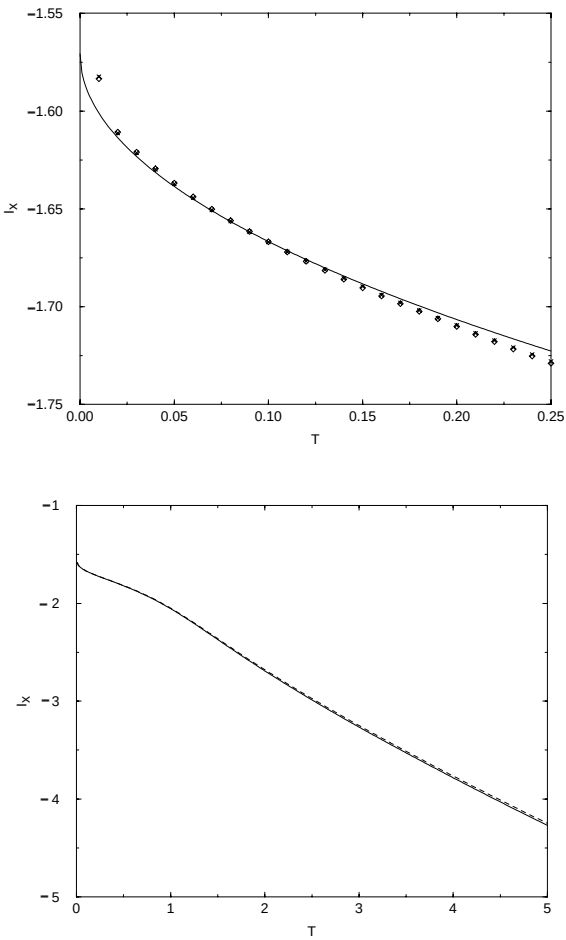

FIG. 20. I_x comparison for an impulsively started circular cylinder, at Re = 550. Short time (top): analytical (solid line), uniform KL-like (◇), nonuniform KL-like (×). Long time (bottom): uniform KL-like (solid line), nonuniform KL-like (dashed line).

$(i + k, j + l)$, with (k, l) in $[-n_l, n_l] \times [-n_l, n_l]$, falls inside the body, the presence of a particle at position (i, j) is guaranteed.

A redistribution is performed every five time steps, and the presence of a layer of 10 particles around the body is enforced. When one uses the nonuniform scheme for long-time computations, it is no longer valid to delete new particles with $|\Gamma| < \varepsilon|\Gamma|_{\max}$, because, for long-time simulations, $|\Gamma|_{\max}$ corresponds to a particle located in the far wake, whose circulation might be very large because the surface associated with that particle is very large. A better approach consists in deleting all particles with $|\Gamma| < \varepsilon|\Gamma|_{\max}$ *and* $|\Gamma| < \Gamma_{\text{trsh}}$ (i.e., satisfy both a relative criterion and an absolute criterion). For short times, the first criterion will be effective, and for long times, it is the second one that will come into play. To choose an appropriate value for Γ_{trsh}, one has to consider the mesh Reynolds number based on vorticity: $\text{Re}_h = |\omega|h^2/\nu$. Since particle strengths correspond to $\Gamma = \omega h^2$, we have $\text{Re}_h = \frac{|\Gamma|}{\nu}$. Tests have shown that a "good" value for Γ_{trsh} corresponds to $\text{Re}_{h,\text{trsh}} = \Gamma_{\text{trsh}}/\nu = 10^{-4}$. Thus, particles for which the "mesh" Reynolds number is really very low are deleted. For S_1 and S_2, the values $\Gamma_{\text{trsh}} = 10^{-4}\,\nu$ and $\varepsilon = 10^{-4}$ were used. All the others parameters are similar

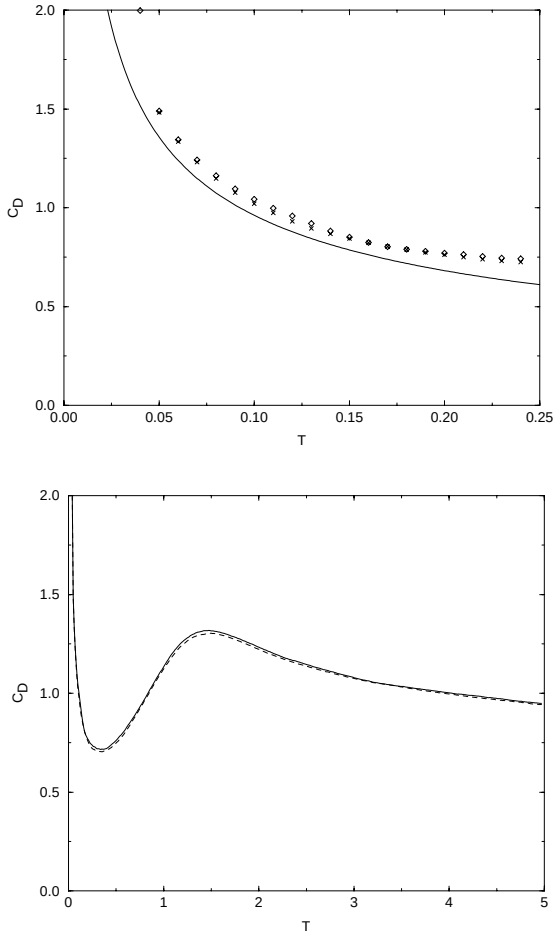

FIG. 21. C_D comparison for an impulsively started circular cylinder, at Re $= 550$. Short time (top): analytical (solid line), uniform KL-like ($\diamond$), nonuniform KL-like ($\times$). Long time (bottom): uniform KL-like (solid line), nonuniform KL-like (dashed line).

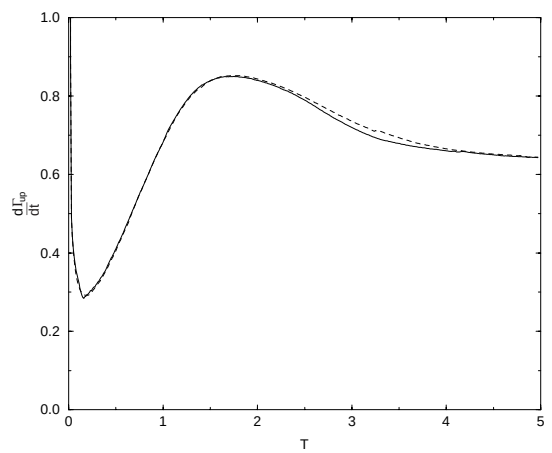

FIG. 22. $d\Gamma_{\text{up}}/dt$ comparison for an impulsively started circular cylinder, at Re $= 550$: uniform KL-like (solid line), nonuniform KL-like (dashed line).

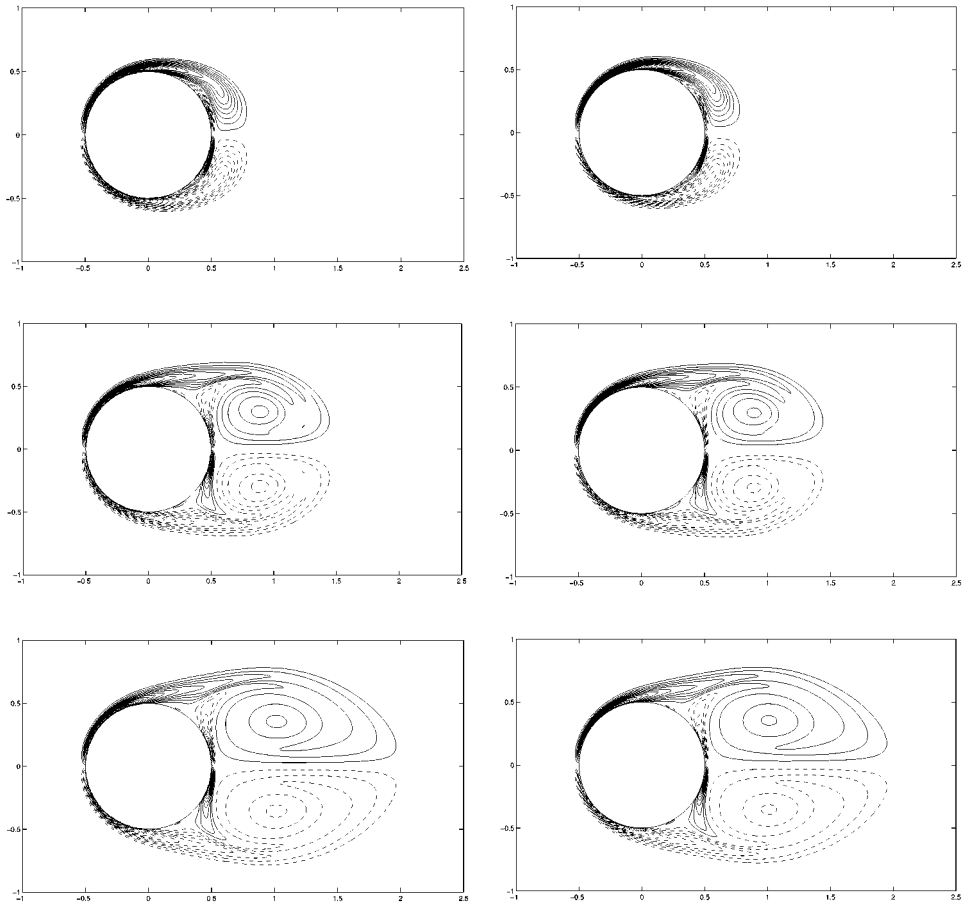

FIG. 23. Iso contours of vorticity for $T = 1, 3$, and 5 for an impulsively started circular cylinder, at $\mathrm{Re} = 550$: uniform KL-like (left), nonuniform KL-like (right). Levels are by steps of 2 (zero level is skipped).

to those presented in Section 4.1. Figure 31 shows the evolution of the drag coefficient and of the number of particles for S_1 and S_2. These two runs have $\mathrm{Re}_h \sim 1$ close to the wall, but the evolution of the resolution varies differently in space for the two methods. At the end of the simulations, the maximum value of Re_h (corresponding to the far-wake particles) is $\sim$25 for S_1 and $\sim$11 for S_2. This means that the far wake is under-resolved in S_1 but has a better (and fair) resolution in S_2. This under-resolution of the far wake is, of course, controlable by displacing the center (x_0, y_0) of the redistribution lattice. This is precisely what was done in S_2. The center (x_0, y_0) can be further modified. Iso contours of vorticity from the simulation S_2 are shown in Fig. 32; they correspond to a region close to the body where $\mathrm{Re}_h \leq 2$. Figure 33 shows isocontours even closer to the body, also for S_2, illustrating the fine resolution.

7. FLOW PAST AN IMPULSIVELY STARTED 2-D "APOLLO" CAPSULE

In this section, the flow past an impulsively started 2-D "Apollo" capsule of generic shape is considered. The justification for the study of such a 2-D flow can be found in

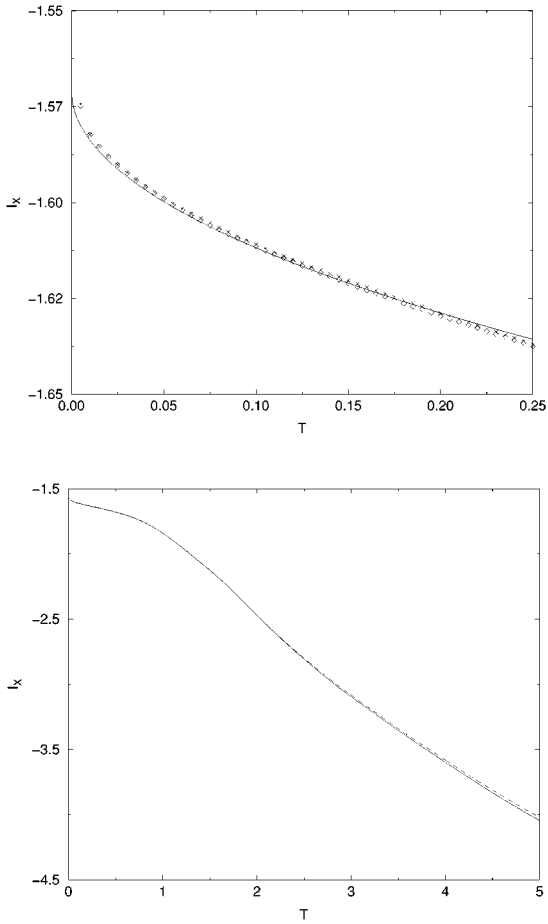

FIG. 24. I_x comparison for an impulsively started circular cylinder, at Re = 3000. Short time (top): analytical (solid line), uniform KL-like (◇), nonuniform KL-like (×). Long time (bottom): uniform KL-like (solid line), nonuniform KL-like (dashed line).

Wang, *et al.* [17]. This geometry offers the opportunity to compute the flow past a body whose geometry is not trivial. The Reynolds number is $\mathrm{Re} = U_\infty D/\nu = 1500$, where D is the width of the capsule. The angle of attack is 40°, and the time step is $\Delta T = 0.005$. The mapping used for the computation is centered at $(x_0, y_0) = (-0.6, 0)$ and has $m = 1000$. This is illustrated in Fig. 34, where the value $m = 200$ has been used for clarity of the figure. Figure 34 also shows the initial position of the particles along with a closeup of the mapping drawn, this time, with $m = 1000$. In the course of the simulation, the number of particles grows from ∼15,000 to ∼108,000. All the other parameters are the same as those used in Section 6. The evolution of the drag and lift coefficients is shown in Fig. 35. It is interesting to note the mean values: $\bar{C}_\mathrm{D} = 1.91$, $\bar{C}_\mathrm{L} = 0.69$, and $\mathrm{St} = fD/U_\infty = 0.135$, the Strouhal number for vortex shedding. These are in good agreement with those obtained in tests of the same 2-D configuration in a water tunnel (O. Karatekin, 2000, private communication). Isocontours of the vorticity are shown in Figs. 36 and 37. In the domain shown in Fig. 36, the "mesh" Reynolds number, Re_h, is everywhere less than 75.

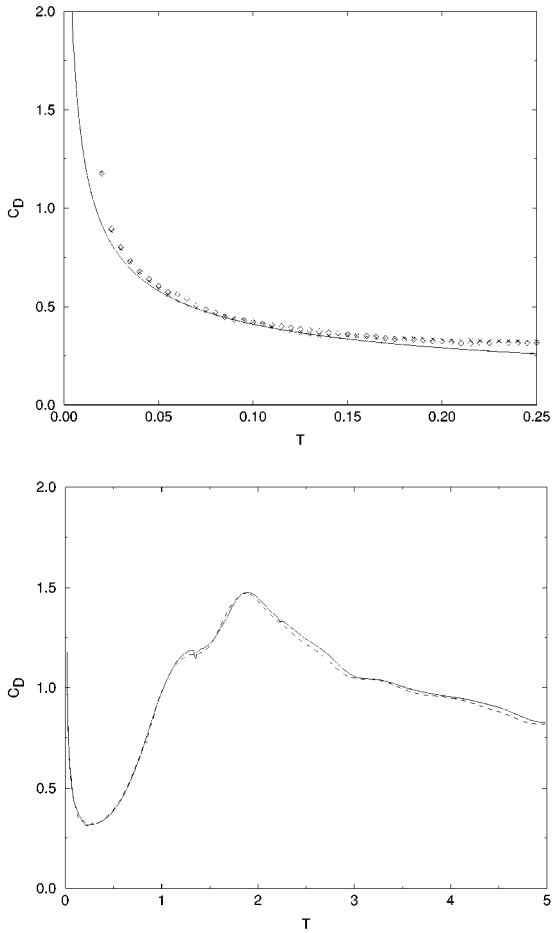

FIG. 25. C_D comparison for an impulsively started circular cylinder, at Re $= 3000$. Short time (top): analytical (solid line), uniform KL-like ($\diamond$), nonuniform KL-like ($\times$). Long time (bottom): uniform KL-like (solid line), nonuniform KL-like (dashed line).

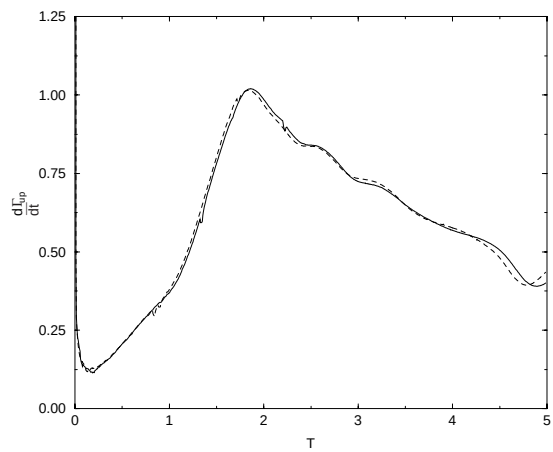

FIG. 26. $d\Gamma_{up}/dt$ comparison for an impulsively started circular cylinder, at Re $= 3000$: uniform KL-like (solid line), nonuniform KL-like (dashed line).

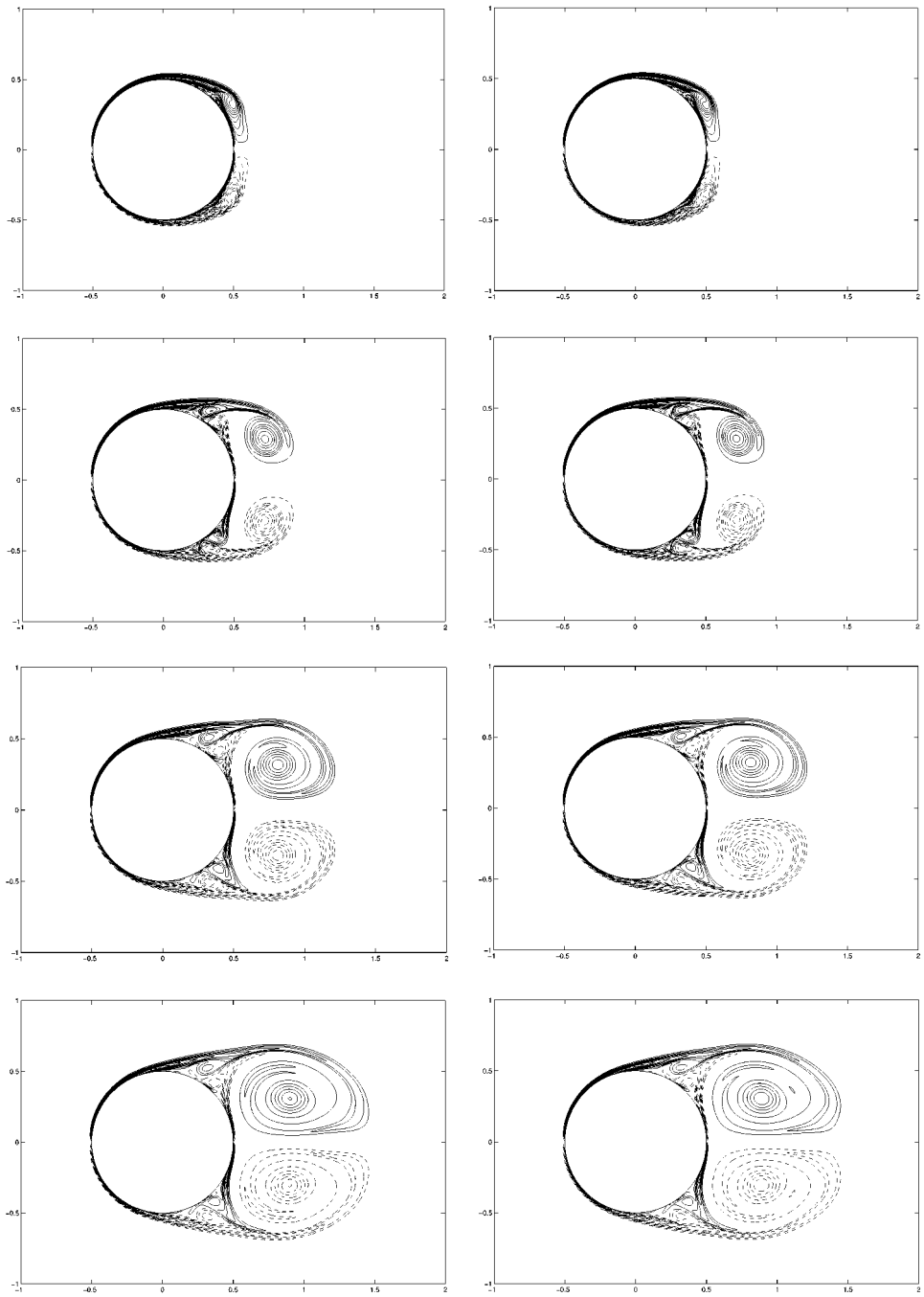

FIG. 27. Iso contours of vorticity for $T = 1, 2, 3$, and 4 for an impulsively started circular cylinder, at $\mathrm{Re} = 3000$: uniform KL-like (left), nonuniform KL-like (right). Levels are by steps of 4 (zero level is skipped).

The right part of the graph is thus underresolved. However, in the region covered by Fig. 37, Re_h is always less than 6, this value being reached around $(X, Y) = (-1.1, 0.2)$, where the vorticity magnitude is very high. The fact that relatively high values of Re_h are reached in the far wake means that, in this region of the flow, the Navier–Stokes equations are not solved

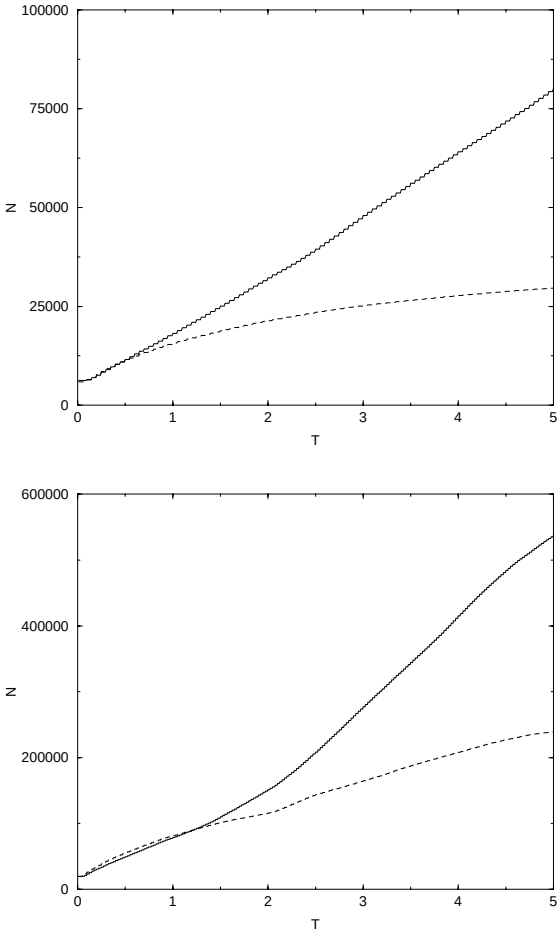

FIG. 28. Evolution of the number of particles as a function of time for an impulsively started circular cylinder. Re = 550 (top): uniform KL-like (solid line), nonuniform KL-like (dashed line); Re = 3000 (bottom): uniform KL-like (solid line), nonuniform KL-like (dashed line).

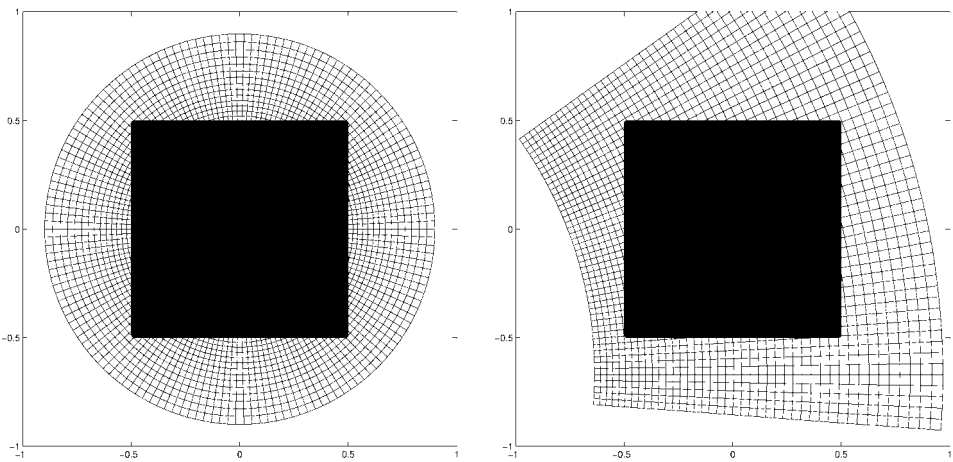

FIG. 29. The two redistribution mappings for the flow past a square; $m = 150$, $(x_0, y_0) = (0, 0)$ (left); $m = 425$, $(x_0, y_0) = (-2.5, -0.67)$ (right).

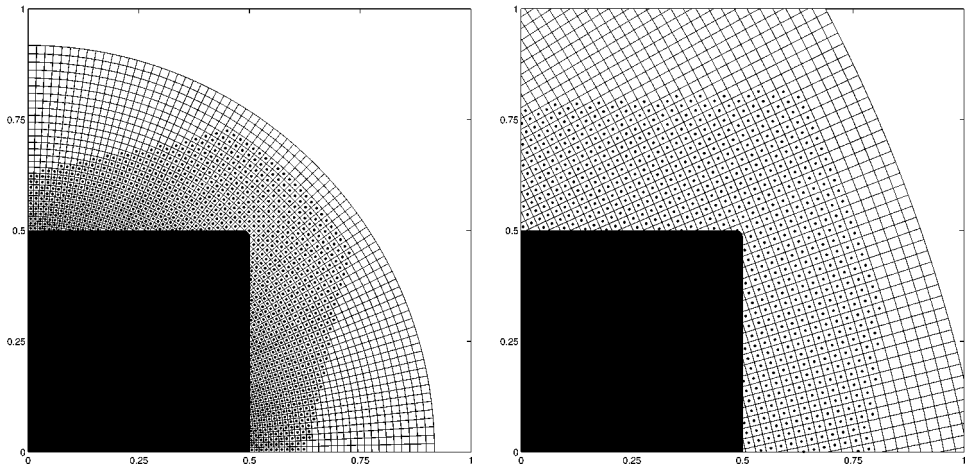

FIG. 30. The two initial situations for the flow past a square at Re $= 100$; $m = 300$, $(x_0, y_0) = (0, 0)$ (left); $m = 850$, $(x_0, y_0) = (-2.5, -0.67)$ (right).

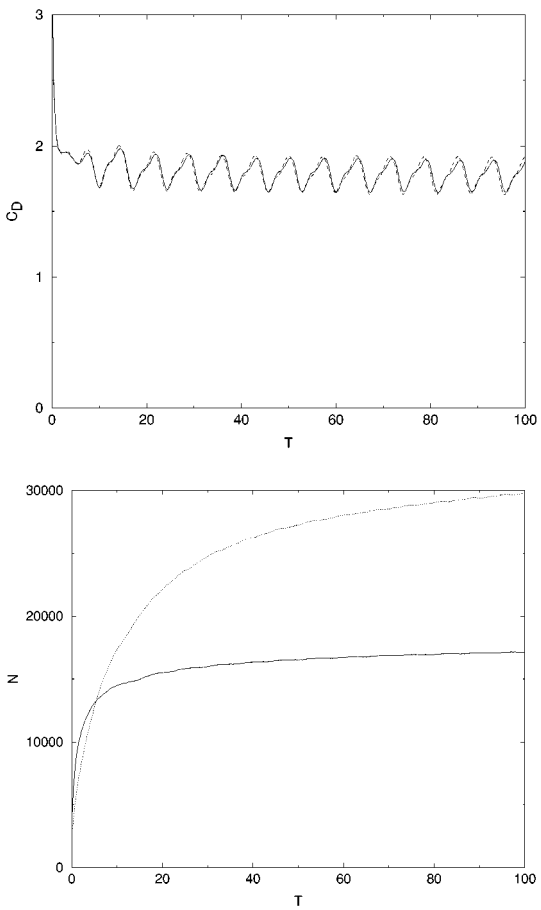

FIG. 31. Flow past a square at 15° and Re $= 100$: evolution of the drag coefficient (top) and of the number of particles (bottom) for S_1 (solid line) and S_2 (dashed line).

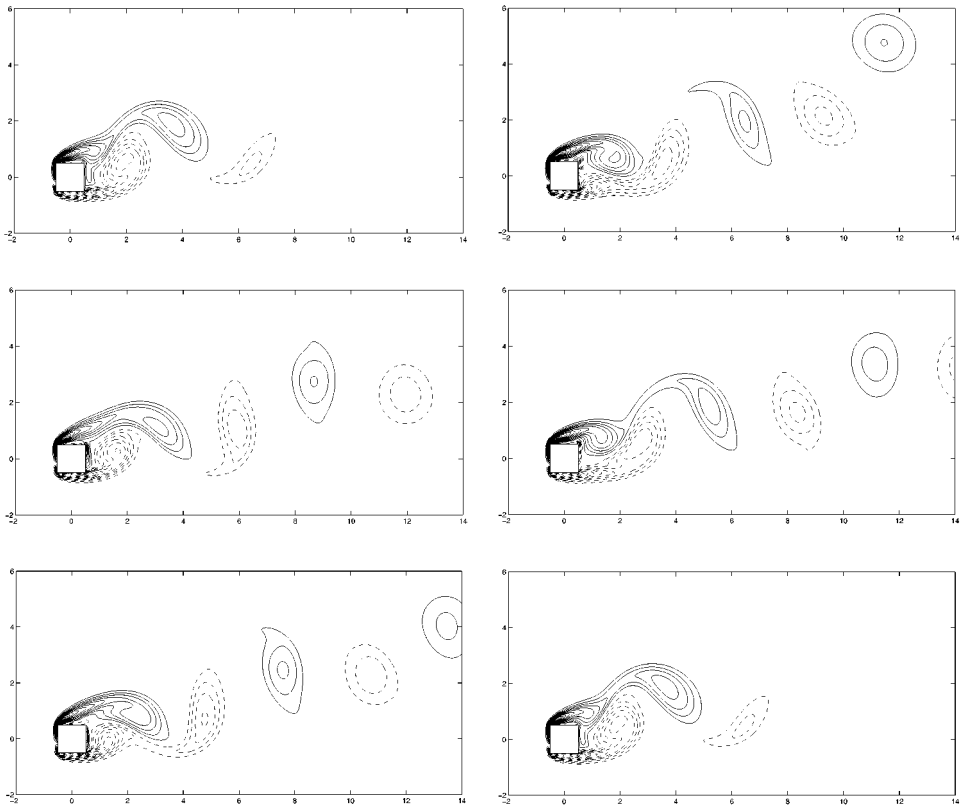

FIG. 32. Flow past a square at 15° and Re = 100 using S_2 redistribution lattice: iso contours of vorticity for $T = 10, 20, 30, 40, 50, 100$ (top to bottom, left to right). Levels are by steps of 0.5.

accurately. The far-wake computation should thus be viewed as a kind of "outflow boundary condition."

8. STRAIGHTFORWARD PARTICLE REDISTRIBUTION

A redistribution technique, which is simpler than the one presented in Section 3.5, was suggested by one of the reviewers of the present paper.

In this approach, straightforward redistribution is applied to all the particles (using, say, a Λ_3 scheme), and newly created particles that would fall into the body are deleted. In general, such an approach does not conserve any moment of the vorticity field, but the reviewer suggested that it could be plausible that the crude treatment given to particles close to the boundary "only provides the overall vortex scheme with some artificial boundary condition that the vortex sheet algorithm corrects afterwards by injecting in the fluid the right amount of vorticity."

This redistribution technique will be referred to hereafter as SF, and the overall vortex scheme using SF for the redistribution will be named G + SF. The new scheme has been tested on two problems:

- the flow past an impulsively started cylinder, at Re = 550;

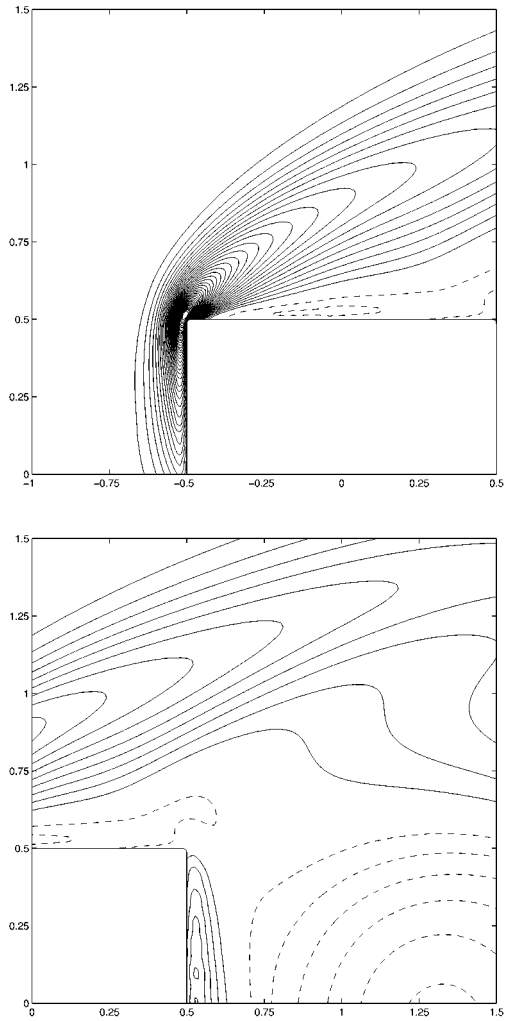

FIG. 33. Flow past a square at 15° and Re = 100 using S_2 redistribution lattice: iso contours of vorticity for $T = 100$. Levels are by steps of 0.5.

• the flow past an impulsively started square, at Re = 100, angle of attack of 15°, and nonuniform resolution.

8.1. *Flow Past a Cylinder*

The flow past a cylinder, at Re = 550, is used to test the SF scheme. All the numerical parameters of the simulation are the same as those used for the same flow in Section 4.1. Because of the symmetry of this flow, the vorticity is an odd function of y,

$$\omega(x, -y) = -\omega(x, y). \tag{51}$$

Consequently, using the SF scheme does not change the total vorticity of the flow: if a newly created particle with $y > 0$ falls inside the body (and is thus deleted), another particle, with $y < 0$ and vorticity of opposite sign, is also deleted. The two errors cancel each other.

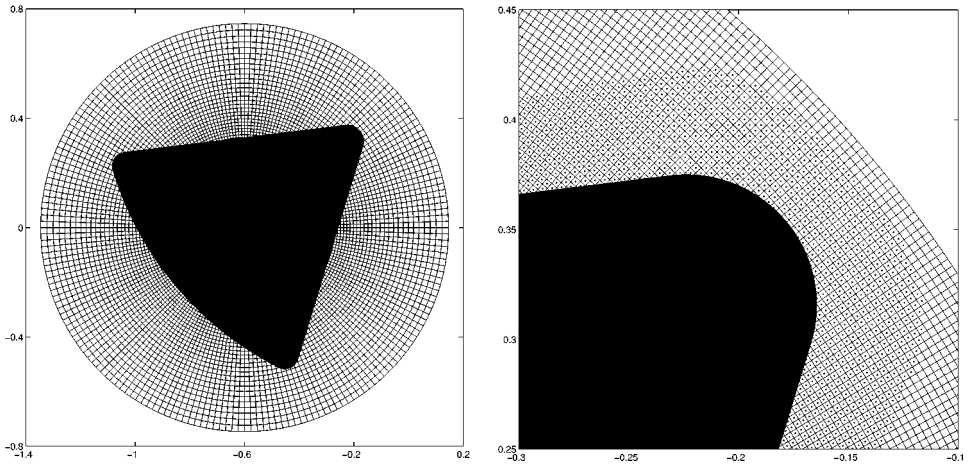

FIG. 34. Redistribution mapping for the flow past an "Apollo" capsule at 40°, with $m = 200$ (left). Initial situation for the flow at $\mathrm{Re} = 1500$ and mapping drawn with $m = 1000$ (right).

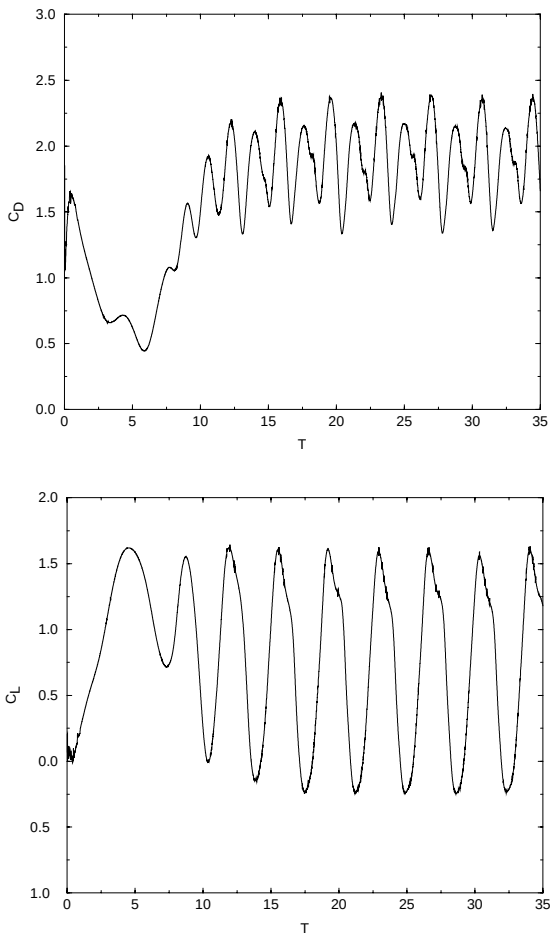

FIG. 35. Flow past an "Apollo" capsule at 40° and $\mathrm{Re} = 1500$: evolution of the drag coefficient (top) and lift coefficient (bottom).

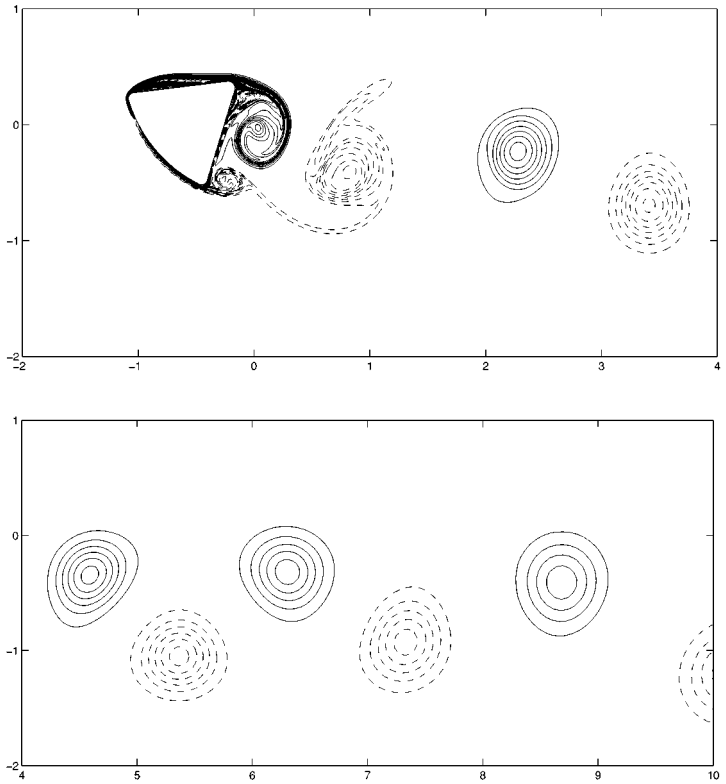

FIG. 36. Flow past an "Apollo" capsule at 40° and Re = 1500: iso contours of vorticity at $T = 35$. Levels are by steps of 2.

However, the linear impulse, $I_x = \int_\Omega y\omega \, d\Omega$, will be affected, since $y\omega$ is an even function of y. This is illustrated in Fig. 38, where the methods G and G + SF are compared for both short and long times. The jumps that occur in the curves every five time steps are due to SF not conserving the first order of the vorticity field. The drag coefficients from the two methods are compared in Fig. 39 (the spurious data in the linear impulse have been removed prior to the numerical differentiation).

It is seen that methods G and G + SF give very similar results on this flow. This indicates that the vortex sheet algorithm performs remarkably well in helping the method recover from the crudeness inherent in SF.

8.2. *Flow Past a Square*

The flow past a square at Re = 100, with angle of attack 15° and nonuniform resolution, is now considered, using the same parameters as those used for run S_2 of Section 6. The nonzero angle of attack makes this flow nonsymmetric; the use of SF will therefore modify the total vorticity.

Methods G and G + SF have been used to compute this flow. The resultant drag coefficient, C_D, has been plotted in Fig. 40. It is hardly possible to see any difference between these two curves, which indicates, once again, that the vortex sheet algorithm makes a very good job at correcting the spurious effects of SF.

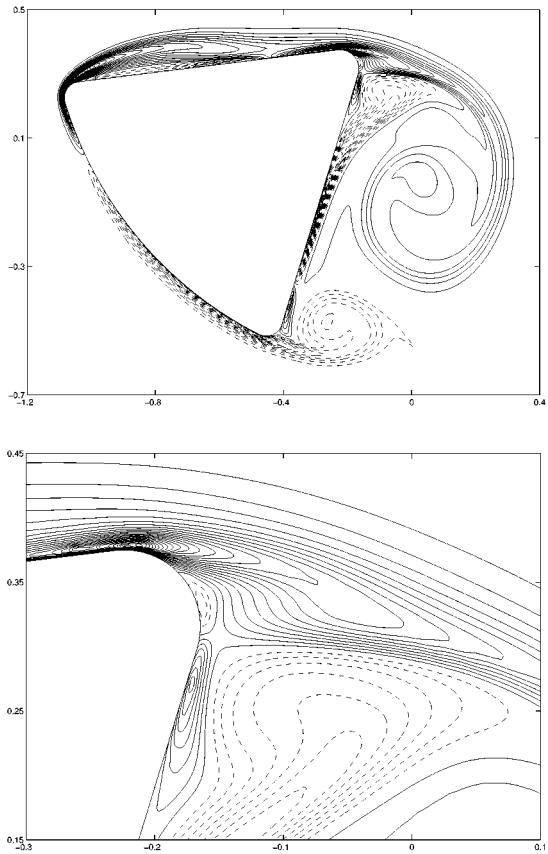

FIG. 37. Flow past an "Apollo" capsule at 40° and Re = 1500: iso contours of vorticity at $T = 35$. Levels are by steps of 4.

9. CONCLUSIONS

• A technique to redistribute particles in the presence of bodies of general geometry was developed and validated. It uses a combination of high-order redistribution schemes, thereby conserving the total vorticity, the linear impulse, and the angular impulse.

• A modified particle strength exchange (PSE) scheme was used near the solid boundaries: it uses image particles to guarantee a zero vorticity flux at the boundary during the PSE substep.

• The no-slip boundary condition is enforced in two steps: a vortex sheet that cancels the slip velocity is first computed; it is then diffused onto nearby particles. The diffusion scheme presented herein is a more accurate version of the original method developed by Koumoutsakos *et al.* [8]. It makes the method conservative (i.e., it guarantees that the vortex sheet is now exactly diffused into the flow). Notice that, besides its being of interest from the point of view of accuracy, the new scheme has the additional property that it allows one to perform under-resolved simulations that still have the proper global vorticity flux from the boundary.

• A mapping of the redistribution lattice was integrated into the present method, making it possible to compute the far wake of bluff-body flows with a coarser, controllable, resolution.

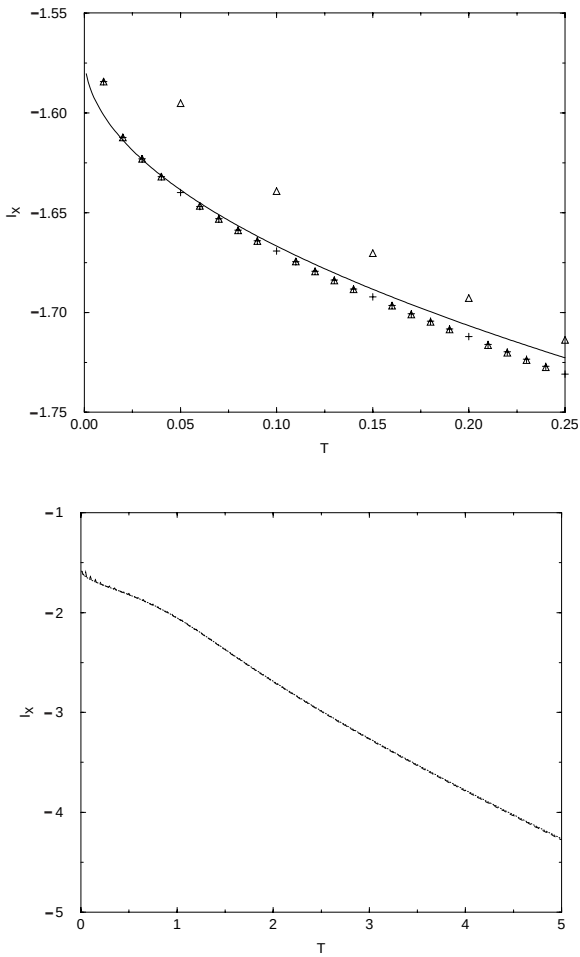

FIG. 38. I_x comparison for an impulsively started circular cylinder, at Re $= 550$. Short time (top): analytical (solid line), G (+), G + SF (△). Long time (bottom): G (solid line), G + SF (dashed line).

• The flow past an impulsively started circular cylinder was used to validate the "general" method with uniform resolution. It was shown that the new general method performs slightly better if small random "vibrations" are applied to the particle redistribution lattice. It was also shown that, at the same resolution, it performs almost as well as the body-fitted method of Koumoutsakos and Leonard [9]. This result is very encouraging. In addition, a convergence study of the general method was also carried out (in which the spatial resolution was increased and the time step decreased).

• The general method with nonuniform resolution was validated on the same flow, illustrating the interest of using particle redistribution on a nonuniform lattice. Significantly reduced computational cost for a similar level of accuracy was obtained.

• For the case with nonuniform resolution, and thus nonuniform σ, the PSE was modified to be performed in physical space while remaining conservative. The quadratic convergence of the modified scheme was proved mathematically and supported by numerical tests.

• The flow past an impulsively started square at Re $= 100$ and $\alpha = 15^\circ$ was computed. The combination of the general method with the mapping made it possible to simulate this

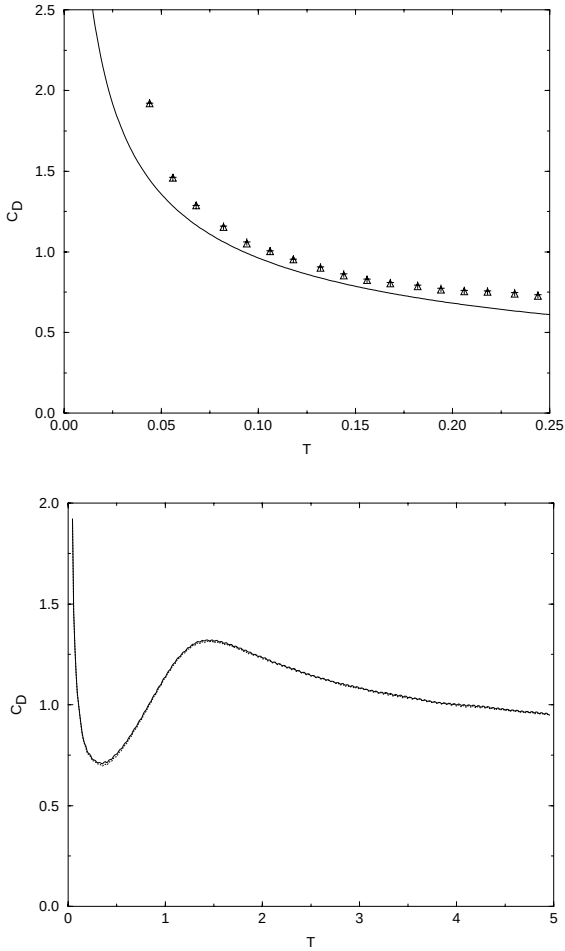

FIG. 39. C_{D} comparison for an impulsively started circular cylinder, at Re $=$ 550. Short time (top): analytical (solid line), G ($+$), G $+$ SF ($\triangle$). Long time (bottom): G (solid line), G $+$ SF (dashed line).

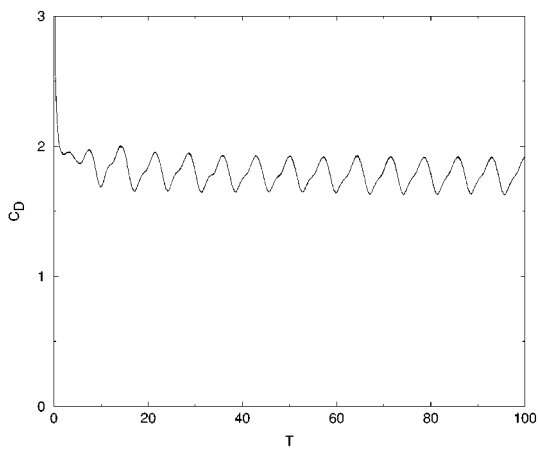

FIG. 40. Flow past a square at 15°and Re $=$ 100: evolution of the drag coefficient (top) for G (solid line) and G $+$ SF (dashed line).

flow up to $T = 100$. If it were to be performed at uniform resolution, such a simulation would require an extremely large number of particles. It was also shown that the parameters of the mapping can be used to control the resolution both near the body and in the far wake.

- The flow past a generic 2-D "Apollo" capsule at Re $= 1500$ and $\alpha = 40^\circ$ was used to demonstrate the capability of the method to compute flows past bluff bodies of truly general geometry for extended times ($T = 35$).
- A very simple particle redistribution technique, suggested by one of the reviewers, was also tested. Although it lacks a sound theoretical basis and relies heavily on the robustness of the overall vortex scheme (especially the vortex sheet algorithm), it performed very well on the flows upon which it was tested.

APPENDIX A

Proof of the Convergence of the PSE with Variable Core Size

In 2-D, the particle strength exchange scheme is based on the approximation of the Laplacian operator by the integral operator

$$\frac{\partial^2 f(\mathbf{x})}{\partial x_r \partial x_r} \simeq \frac{2}{\sigma^2} \int (f(\mathbf{y}) - f(\mathbf{x}))\eta\left(\frac{|\mathbf{y}-\mathbf{x}|}{\sigma}\right)\frac{d\mathbf{y}}{\sigma^2} \tag{A.1}$$

with $\eta(|\mathbf{z}|)$ a radially symmetric function such that

$$\int \eta(|\mathbf{z}|)\, d\mathbf{z} = 1 \tag{A.2}$$

$$\int z_i z_j \eta(|\mathbf{z}|)\, d\mathbf{z} = \delta_{ij} \tag{A.3}$$

$$\int \eta(|\mathbf{z}|)\, |\mathbf{z}|^4\, d\mathbf{z} < \infty. \tag{A.4}$$

Equation (A.1) is accurate to second order. To show that, we consider a Taylor expansion of f around $\mathbf{x}$,

$$f(\mathbf{y}) = f(\mathbf{x}) + \frac{\partial f(\mathbf{x})}{\partial x_i}(y_i - x_i) + \frac{1}{2}\frac{\partial^2 f(\mathbf{x})}{\partial x_i \partial x_j}(y_i - x_i)(y_j - x_j) + \frac{1}{6}\frac{\partial^3 f(\mathbf{x})}{\partial x_i \partial x_j \partial x_k} \times (y_i - x_i)(y_j - x_j)(y_k - x_k) + \frac{\partial^4 f(\mathbf{x})}{\partial x_i \partial x_j \partial x_k \partial x_l}\mathcal{O}(|\mathbf{y}-\mathbf{x}|^4), \tag{A.5}$$

with implicit summation on the repeated indices (here running from 1 to 2). If Eq. (A.5) is introduced in Eq. (A.1), and the radial symmetry of η is taken into account, one finds

$$\begin{aligned}
&\frac{2}{\sigma^2}\int (f(\mathbf{y}) - f(\mathbf{x}))\eta\left(\frac{|\mathbf{y}-\mathbf{x}|}{\sigma}\right)\frac{d\mathbf{y}}{\sigma^2} \\
&\quad = \frac{\partial^2 f(\mathbf{x})}{\partial x_i \partial x_j}\int z_i z_j \eta(|\mathbf{z}|)\, d\mathbf{z} + \frac{\partial^4 f(\mathbf{x})}{\partial x_i \partial x_j \partial x_k \partial x_l}\mathcal{O}\left(\sigma^2 \int |\mathbf{z}|^4 \eta(\mathbf{z})\, d\mathbf{z}\right) \\
&\quad = \frac{\partial^2 f(\mathbf{x})}{\partial x_i \partial x_j}\delta_{ij} + \frac{\partial^4 f(\mathbf{x})}{\partial x_i \partial x_j \partial x_k \partial x_l}\mathcal{O}(\sigma^2) \\
&\quad = \frac{\partial^2 f(\mathbf{x})}{\partial x_i \partial x_i} + \frac{\partial^4 f(\mathbf{x})}{\partial x_i \partial x_j \partial x_k \partial x_l}\mathcal{O}(\sigma^2)
\end{aligned} \tag{A.6}$$

with $\mathbf{z} = (\mathbf{y} - \mathbf{x})/\sigma$. The replacement of the Laplacian operator by Eq. (A.1) is thus second-order accurate for uniform σ.

Let us now investigate the influence of a nonuniform σ. If one replaces σ by $\sigma(\mathbf{x})$ in Eq. (A.1), the approximation error is $\mathcal{O}(\sigma^2(\mathbf{x}))$, but the discretized scheme is not conservative.

Another possibility is to replace σ by $\sigma(\mathbf{y})$ in Eq. (A.1):

$$\frac{\partial^2 f(\mathbf{x})}{\partial x_r \partial x_r} \simeq 2 \int \frac{1}{\sigma^2(\mathbf{y})} (f(\mathbf{y}) - f(\mathbf{x})) \eta\left(\frac{|\mathbf{y} - \mathbf{x}|}{\sigma(\mathbf{y})}\right) \frac{d\mathbf{y}}{\sigma^2(\mathbf{y})}. \tag{A.7}$$

Note that, in this equation, σ^2 can also be taken as $\sigma^2 = (\sigma^2(\mathbf{x}) + \sigma^2(\mathbf{y}))/2$, which leads to a conservative discrete scheme. This is what is done in the implementation used in this paper.

It will now be shown that Eq. (A.7) is still second-order accurate. First, one defines

$$\mathbf{z} = \frac{\mathbf{y} - \mathbf{x}}{\sigma(\mathbf{y})} = \mathbf{z}(\mathbf{y}, \mathbf{x}) \tag{A.8}$$

and assumes that $\mathbf{y}$ can be recovered from $\mathbf{x}$ and $\mathbf{z}$; i.e., $\mathbf{y} = \mathbf{y}(\mathbf{x}, \mathbf{z})$. In Eq. (A.7), it is necessary to use $\mathbf{z}$ as the integration variable. One has

$$d\mathbf{z} = J \, d\mathbf{y}, \tag{A.9}$$

where J is the jacobian of the coordinate transformation

$$J = J(\mathbf{y}) = \det\left(\frac{\partial z_i}{\partial y_j}\right), \tag{A.10}$$

with

$$\frac{\partial \mathbf{z}}{\partial \mathbf{y}}(\mathbf{y}) = \frac{1}{\sigma} \begin{pmatrix} 1 - z_1 \partial_1 \sigma & -z_1 \partial_2 \sigma \\ -z_2 \partial_1 \sigma & 1 - z_2 \partial_2 \sigma \end{pmatrix} \tag{A.11}$$

$$\frac{\partial z_i}{\partial y_j} = \frac{1}{\sigma} (\delta_{ij} - z_i \partial_j \sigma), \tag{A.12}$$

where $\partial_i \sigma = \partial \sigma / \partial y_i$. Hence, one has, for the jacobian,

$$J = \frac{1}{\sigma^2} (1 - z_k \partial_k \sigma). \tag{A.13}$$

The transformation can be inverted to give

$$\frac{\partial \mathbf{y}}{\partial \mathbf{z}}(\mathbf{y}) = \frac{\sigma}{1 - z_k \partial_k \sigma} \begin{pmatrix} 1 - z_2 \partial_2 \sigma & z_1 \partial_2 \sigma \\ z_2 \partial_1 \sigma & 1 - z_1 \partial_1 \sigma \end{pmatrix}, \tag{A.14}$$

which can be written in a more condensed form,

$$\frac{\partial y_i}{\partial z_j} = \frac{\sigma}{1 - z_k \partial_k \sigma} \alpha_{ij}, \tag{A.15}$$

with

$$\alpha = \begin{pmatrix} 1 - z_2\partial_2\sigma & z_1\partial_2\sigma \\ z_2\partial_1\sigma & 1 - z_1\partial_1\sigma \end{pmatrix}. \tag{A.16}$$

A useful property of α_{ij} is

$$\partial_j \sigma \alpha_{ji} = \partial_i \sigma. \tag{A.17}$$

The terms of Eq. (A.5) are now introduced into Eq. (A.7). One has

$$\int \frac{1}{\sigma^2(\mathbf{y})}(f(\mathbf{y}) - f(\mathbf{x}))\eta\left(\frac{|\mathbf{y}-\mathbf{x}|}{\sigma(\mathbf{y})}\right)\frac{d\mathbf{y}}{\sigma^2(\mathbf{y})} = I_1 + I_2 + I_3 + I_4, \tag{A.18}$$

with

$$I_1 = 2\frac{\partial f(\mathbf{x})}{\partial x_i}\int \frac{1}{\sigma(1 - z_m\partial_m\sigma)} z_i \eta(|\mathbf{z}|)\, d\mathbf{z} \tag{A.19}$$

$$I_2 = \frac{\partial^2 f(\mathbf{x})}{\partial x_i \partial x_j}\int \frac{1}{(1 - z_m\partial_m\sigma)} z_i z_j \eta(|\mathbf{z}|)\, d\mathbf{z} \tag{A.20}$$

$$I_3 = \frac{1}{3}\frac{\partial^3 f(\mathbf{x})}{\partial x_i \partial x_j \partial x_k}\int \frac{\sigma}{(1 - z_m\partial_m\sigma)} z_i z_j z_k \eta(|\mathbf{z}|)\, d\mathbf{z} \tag{A.21}$$

$$I_4 = \frac{\partial^4 f(\mathbf{x})}{\partial x_i \partial x_j \partial x_k \partial x_l}\mathcal{O}\left(\int \frac{\sigma^2}{(1 - z_m\partial_m\sigma)} \eta(|\mathbf{z}|)|\mathbf{z}|^4\, d\mathbf{z}\right), \tag{A.22}$$

where σ has been written instead of $\sigma(\mathbf{x}, \mathbf{z})$. In what follows, σ will be written as

$$\sigma(\mathbf{y}) = \epsilon g\left(\frac{\mathbf{y}}{L}\right) = \epsilon g(\boldsymbol{\zeta}), \tag{A.23}$$

with L a global length scale and $g(\boldsymbol{\zeta})$ a smooth function with $g(\boldsymbol{\zeta}) = \mathcal{O}(1)$. Because of the smoothness of g, all its derivatives are also $\mathcal{O}(1)$. Consequently, one has

$$\sigma = \mathcal{O}(\epsilon) = L\mathcal{O}\left(\frac{\epsilon}{L}\right) \tag{A.24}$$

$$\begin{aligned} \partial_i\sigma &= \frac{\partial\sigma}{\partial y_i} = \epsilon\frac{\partial g}{\partial\zeta_j}\frac{\partial\zeta_j}{\partial y_i} \\ &= \frac{\epsilon}{L}\frac{\partial g}{\partial\zeta_i} = \mathcal{O}\left(\frac{\epsilon}{L}\right) \end{aligned} \tag{A.25}$$

$$\begin{aligned} \partial^2_{ij}\sigma &= \frac{\epsilon}{L}\frac{\partial^2 g}{\partial\zeta_i\partial\zeta_k}\frac{\partial\zeta_k}{\partial y_j} \\ &= \frac{\epsilon}{L^2}\frac{\partial^2 g}{\partial\zeta_i\partial\zeta_j} = \frac{1}{L}\mathcal{O}\left(\frac{\epsilon}{L}\right). \end{aligned} \tag{A.26}$$

All the I_i's will now be developed around $\mathbf{z} = \mathbf{0}$ (i.e., around $\mathbf{y} = \mathbf{x}$).

I_1 Term

One defines

$$K^1(\mathbf{y}) = K^1 = \frac{1}{\sigma(1 - z_m \partial_m \sigma)} \tag{A.27}$$

and performs a Taylor development of K^1 around $\mathbf{z} = \mathbf{0}$:

$$\begin{aligned} K^1(\mathbf{y}) = K^1|_{\mathbf{z}=\mathbf{0}} &+ \left.\frac{\partial K^1}{\partial z_i}\right|_{\mathbf{z}=\mathbf{0}} z_i + \frac{1}{2}\left.\frac{\partial^2 K^1}{\partial z_i \partial z_j}\right|_{\mathbf{z}=\mathbf{0}} z_i z_j \\ &+ \frac{1}{6}\left.\frac{\partial^3 K^1}{\partial z_i\, \partial z_j\, \partial z_k}\right|_{\mathbf{z}=\mathbf{0}} z_i z_j z_k + \left.\frac{\partial^4 K^1}{\partial z_i\, \partial z_j\, \partial z_k\, \partial z_l}\right|_{\mathbf{z}=\mathbf{0}} \mathcal{O}(|\mathbf{z}|^4). \end{aligned} \tag{A.28}$$

The first term,

$$K^1|_{\mathbf{z}=\mathbf{0}} = \left.\frac{1}{\sigma}\right|_{\mathbf{y}=\mathbf{x}}, \tag{A.29}$$

does not contribute to I_1, because of the radial symmetry of η. The first derivative of K^1 is

$$\frac{\partial K^1}{\partial z_i} = \frac{\partial K^1}{\partial y_j}\frac{\partial y_j}{\partial z_i}, \tag{A.30}$$

with

$$\begin{aligned} \frac{\partial K^1}{\partial y_j} &= -\frac{1}{\sigma^2(1 - z_k\partial_k\sigma)^2} \cdot \left(\partial_j\sigma(1 - z_m\partial_m\sigma) + \sigma\left(-\frac{\partial z_m}{\partial y_j}\partial_m\sigma - z_m\partial^2_{mj}\sigma\right)\right) \\ &= -\frac{1}{\sigma^2(1 - z_k\partial_k\sigma)^2} \cdot \left(\partial_j\sigma(1 - z_m\partial_m\sigma) + \sigma\left(-\frac{1}{\sigma}(\delta_{mj} - z_m\partial_j\sigma)\partial_m\sigma - z_m\partial^2_{mj}\sigma\right)\right) \\ &= -\frac{1}{\sigma^2(1 - z_k\partial_k\sigma)^2} \cdot \Bigg(\underbrace{\partial_j\sigma - z_m\partial_m\sigma\partial_j\sigma - \partial_j\sigma + z_m\partial_j\sigma\partial_m\sigma}_{=0} - \sigma z_m\partial^2_{mj}\sigma\Bigg) \end{aligned} \tag{A.31}$$

$$= \frac{z_m\partial^2_{mj}\sigma}{\sigma(1 - z_k\partial_k\sigma)^2}. \tag{A.32}$$

Hence, from Eq. (A.15) and Eq. (A.30), one finally finds

$$\frac{\partial K^1}{\partial z_i} = \frac{\partial^2_{mj}\sigma\alpha_{ji}z_m}{(1 - z_k\partial_k\sigma)^3} \tag{A.33}$$

and

$$\left.\frac{\partial K^1}{\partial z_i}\right|_{\mathbf{z}=\mathbf{0}} = 0. \tag{A.34}$$

It is interesting to observe that

$$K^1 = \frac{1}{L}\mathcal{O}\left(\frac{L}{\epsilon}\right) \tag{A.35}$$

and that the application of the operator $\partial/\partial z_i$ multiplies the order by ϵ/L. If the two $\partial_j\sigma$ terms in Eq. (A.31) had not canceled each other, one would have obtained

$$\frac{\partial K^1}{\partial z_i} = \frac{1}{L}\mathcal{O}(1), \tag{A.36}$$

even for $\mathbf{z} = \mathbf{0}$, and I_1 would not vanish as ϵ/L tends to zero, thereby making Eq. (A.7) a nonconvergent approximation of the Laplacian operator. However, because of the cancellation of the $\partial_j\sigma$ terms in Eq. (A.31), one actually obtains

$$\frac{\partial K^1}{\partial z_i} = \frac{1}{L}\mathcal{O}\left(\frac{\epsilon}{L}\right). \tag{A.37}$$

Consequently, one also obtains

$$\left.\frac{\partial^2 K^1}{\partial z_i \partial z_j}\right|_{\mathbf{z}=\mathbf{0}} = \frac{1}{L}\mathcal{O}\left(\left(\frac{\epsilon}{L}\right)^2\right) \tag{A.38}$$

$$\left.\frac{\partial^3 K^1}{\partial z_i \partial z_j \partial z_k}\right|_{\mathbf{z}=\mathbf{0}} = \frac{1}{L}\mathcal{O}\left(\left(\frac{\epsilon}{L}\right)^3\right). \tag{A.39}$$

Because of the radial symmetry of η, Eq. (A.38) does not contribute to I_1, which is finally obtained as

$$I_1 = \frac{\partial f}{\partial x_i}\frac{1}{L}\mathcal{O}\left(\left(\frac{\epsilon}{L}\right)^3 \int |\mathbf{z}|^4 \eta(|\mathbf{z}|)\, dz\right) = \frac{\partial f}{\partial x_i}\frac{1}{L}\mathcal{O}\left(\left(\frac{\epsilon}{L}\right)^3\right), \tag{A.40}$$

where Eq. (A.4) has been used to obtain the last result.

I_2 Term

One defines

$$K^2(\mathbf{y}) = K^2 = \sigma K^1 = \frac{1}{(1 - z_m \partial_m \sigma)} \tag{A.41}$$

and performs a Taylor development around $\mathbf{z} = \mathbf{0}$:

$$K^2(\mathbf{y}) = K^2\Big|_{\mathbf{z}=\mathbf{0}} + \left.\frac{\partial K^2}{\partial z_i}\right|_{\mathbf{z}=\mathbf{0}} z_i + \frac{1}{2}\left.\frac{\partial^2 K^2}{\partial z_i \partial z_j}\right|_{\mathbf{z}=\mathbf{0}} z_i\, z_j + \left.\frac{\partial^3 K^2}{\partial z_i \partial z_j \partial z_k}\right|_{\mathbf{z}=\mathbf{0}} \mathcal{O}(|\mathbf{z}|^3). \tag{A.42}$$

One obtains

$$K^2|_{\mathbf{z}=\mathbf{0}} = 1. \tag{A.43}$$

The first derivative is obtained as

$$\begin{aligned}\frac{\partial K^2}{\partial z_i} &= -\frac{1}{(1 - z_k \partial_k \sigma)^2}\left(-\delta_{im}\partial_m \sigma - z_m \partial^2_{mn}\sigma \frac{\partial y_n}{\partial z_i}\right) \\ &= \frac{1}{(1 - z_k \partial_k \sigma)^2}\left(\partial_i \sigma + z_m \partial^2_{mn}\sigma \frac{\sigma}{1 - z_l \partial_l \sigma}\alpha_{ni}\right);\end{aligned} \tag{A.44}$$

hence, at $\mathbf{y} = \mathbf{x}$, one has

$$\left.\frac{\partial K^2}{\partial z_i}\right|_{\mathbf{z}=\mathbf{0}} = \partial_i \sigma|_{\mathbf{y}=\mathbf{x}}, \tag{A.45}$$

which does not contribute to I_2, because of the radial symmetry of η. To compute the second derivative, it is convenient to define

$$F_{ij} = \partial^2_{in}\sigma \frac{\sigma}{(1 - z_l \partial_l \sigma)} \alpha_{nj} \tag{A.46}$$

so that

$$\frac{\partial K^2}{\partial z_i} = \frac{1}{(1 - z_k \partial_k \sigma)^2} (\partial_i \sigma + z_m F_{mi}), \tag{A.47}$$

and the second derivative of K^2 is

$$\begin{aligned}\frac{\partial^2 K^2}{\partial z_i \partial z_j} = &-\frac{2}{(1 - z_l \partial_l \sigma)^3} \left(-\delta_{kj}\partial_k \sigma - z_k \partial^2_{ks}\sigma \frac{\partial y_s}{\partial z_j}\right)(\partial_i \sigma + z_n F_{ni}) \\ &+ \frac{1}{(1 - z_l \partial_l \sigma)^2} \left(\partial^2_{ik}\sigma \frac{\partial y_k}{\partial z_j} + \delta_{mj} F_{mi} + z_m \frac{\partial F_{mi}}{\partial z_j}\right).\end{aligned} \tag{A.48}$$

Taking into account that, when $\mathbf{z} = \mathbf{0}$ $(\mathbf{y} = \mathbf{x})$,

$$\alpha_{ij} = \delta_{ij} \tag{A.49}$$

$$\frac{\partial y_i}{\partial z_j} = \sigma \delta_{ij} \tag{A.50}$$

$$F_{ij} = \sigma \partial^2_{il}\sigma \delta_{lj} = \sigma \partial^2_{ij}\sigma, \tag{A.51}$$

one finally obtains

$$\begin{aligned}\left.\frac{\partial^2 K^2}{\partial z_i \partial z_j}\right|_{\mathbf{z}=\mathbf{0}} &= 2(\partial_j \sigma|_{\mathbf{y}=\mathbf{x}} \partial_i \sigma|_{\mathbf{y}=\mathbf{x}}) + \left(\sigma|_{\mathbf{y}=\mathbf{x}} \partial^2_{ik}\sigma|_{\mathbf{y}=\mathbf{x}} \delta_{kj} + \sigma|_{\mathbf{y}=\mathbf{x}} \partial^2_{ji}\sigma|_{\mathbf{y}=\mathbf{x}}\right) \\ &= 2\left(\partial_j \sigma|_{\mathbf{y}=\mathbf{x}} \partial_i \sigma|_{\mathbf{y}=\mathbf{x}} + \sigma|_{\mathbf{y}=\mathbf{x}} \partial^2_{ij}\sigma|_{\mathbf{y}=\mathbf{x}}\right) \\ &= \mathcal{O}\left(\left(\frac{\epsilon}{L}\right)^2\right),\end{aligned} \tag{A.52}$$

where the last result has been obtained from Eqs. (A.24), (A.25), and (A.26). It is thus possible to write I_2 as

$$\begin{aligned}I_2 &= \frac{\partial^2 f(\mathbf{x})}{\partial x_i \partial x_j} \int z_i z_j \eta(|\mathbf{z}|)\, d\mathbf{z} + \frac{\partial^2 f(\mathbf{x})}{\partial x_i \partial x_j} \mathcal{O}\left(\left(\frac{\epsilon}{L}\right)^2 \int |\mathbf{z}|^4 \eta(|\mathbf{z}|)\, d\mathbf{z}\right) \\ &= \frac{\partial^2 f(\mathbf{x})}{\partial x_i \partial x_j} \int z_i z_j \eta(|\mathbf{z}|)\, d\mathbf{z} + \frac{\partial^2 f(\mathbf{x})}{\partial x_i \partial x_j} \mathcal{O}\left(\left(\frac{\epsilon}{L}\right)^2\right) \\ &= \frac{\partial^2 f(\mathbf{x})}{\partial x_i \partial x_i}\left(1 + \mathcal{O}\left(\frac{\epsilon}{L}\right)^2\right).\end{aligned} \tag{A.53}$$

I_3 Term

One defines

$$K^3(\mathbf{y}) = K^3 = \sigma K^2 = \frac{\sigma}{1 - z_m \partial_m \sigma} \tag{A.54}$$

and performs again a Taylor expansion around $\mathbf{z} = \mathbf{0}$:

$$K^3(\mathbf{y}) = K^3\Big|_{\mathbf{z}=\mathbf{0}} + \frac{\partial K^3}{\partial z_i}\Big|_{\mathbf{z}=\mathbf{0}} z_i + \frac{\partial^2 K^3}{\partial z_i \partial z_j}\Big|_{\mathbf{z}=\mathbf{0}} \mathcal{O}(|\mathbf{z}|^2). \tag{A.55}$$

One has

$$K^3|_{\mathbf{z}=\mathbf{0}} = \sigma|_{\mathbf{y}=\mathbf{x}}, \tag{A.56}$$

which does not contribute to I_3 because of the radial symmetry of η. The first derivative of K^3 is

$$\begin{aligned}\frac{\partial K^3}{\partial z_i} = \frac{1}{(1 - z_l \partial_l \sigma)^2} \Bigg(\left(\partial_j \sigma \frac{\partial y_j}{\partial z_i} \right) (1 - z_m \partial_m \sigma) \\ - \sigma \left(-\delta_{im} \partial_m \sigma - z_m \partial^2_{mj} \sigma \frac{\partial y_j}{\partial z_i} \right) \Bigg),\end{aligned} \tag{A.57}$$

and, at $\mathbf{y} = \mathbf{x}$:

$$\begin{aligned}\frac{\partial K^3}{\partial z_i}\Big|_{\mathbf{z}=\mathbf{0}} &= \sigma|_{\mathbf{y}=\mathbf{x}} \partial_j \sigma|_{\mathbf{y}=\mathbf{x}} \delta_{ij} - \sigma|_{\mathbf{y}=\mathbf{x}} (-\partial_i \sigma|_{\mathbf{y}=\mathbf{x}}) \\ &= 2\sigma|_{\mathbf{y}=\mathbf{x}} \partial_i \sigma|_{\mathbf{y}=\mathbf{x}} \\ &= L\mathcal{O}\left(\left(\frac{\epsilon}{L} \right)^2 \right),\end{aligned} \tag{A.58}$$

where the last result is obtained from Eqs. (A.24) and (A.25). Using Eq. (A.4), one finally obtains

$$\begin{aligned}I_3 &= \frac{\partial^3 f(\mathbf{x})}{\partial x_i \partial x_j \partial x_k} L\mathcal{O}\left(\left(\frac{\epsilon}{L} \right)^2 \int \eta(|\mathbf{z}|) |\mathbf{z}|^4 \, d\mathbf{z} \right) \\ &= \frac{\partial^3 f(\mathbf{x})}{\partial x_i \partial x_j \partial x_k} L\mathcal{O}\left(\left(\frac{\epsilon}{L} \right)^2 \right).\end{aligned} \tag{A.59}$$

I_4 Term

Starting from Eq. (A.22), one easily observes that

$$I_4 = \frac{\partial^4 f(\mathbf{x})}{\partial x_i \partial x_j \partial x_k \partial x_l} L^2 \mathcal{O}\left(\left(\frac{\epsilon}{L} \right)^2 \right). \tag{A.60}$$

Summary

It has been shown that

$$\int \frac{1}{\sigma^2(\mathbf{y})} \left(f(\mathbf{y}) - f(\mathbf{x})\right) \eta\left(\frac{|\mathbf{y}-\mathbf{x}|}{\sigma(\mathbf{y})}\right) \frac{d\mathbf{y}}{\sigma^2(\mathbf{y})} \tag{A.61}$$

$$= \frac{\partial f}{\partial x_i}\frac{1}{L}\mathcal{O}\left(\left(\frac{\epsilon}{L}\right)^3\right) + \frac{\partial^2 f(\mathbf{x})}{\partial x_i \partial x_i}\left(1 + \mathcal{O}\left(\frac{\epsilon}{L}\right)^2\right)$$

$$+ \frac{\partial^3 f(\mathbf{x})}{\partial x_i \partial x_j \partial x_k} L\mathcal{O}\left(\left(\frac{\epsilon}{L}\right)^2\right) + \frac{\partial^4 f(\mathbf{x})}{\partial x_i \partial x_j \partial x_k \partial x_l} L^2 \mathcal{O}\left(\left(\frac{\epsilon}{L}\right)^2\right). \tag{A.62}$$

Equation (A.7) thus defines a convergent, second-order-accurate approximation of the Laplacian operator.

The use of $\sigma^2 = (\sigma^2(\mathbf{x}) + \sigma^2(\mathbf{y}))/2$ in Eq. (A.7) falls into the category of admissible variation of σ, as it has the form $\sigma = \sigma(\mathbf{y})$ (since $\mathbf{x}$ is fixed in the analysis). Thus, it also leads to a convergent, second-order-accurate approximation. Furthermore, this choice of σ makes the discrete scheme conservative. It is what was used in the numerical implementation.

Finally, the analysis also shows that, when σ is uniform in space, $I_1 = I_3 = 0$, $I_2 = \nabla^2 f(\mathbf{x})$, and I_4 is $\mathcal{O}((\epsilon/L)^2)$.

APPENDIX B

Numerical Convergence of the PSE with Variable Core Size

The convergence of the discretized PSE is illustrated on a test problem. A Gaussian vorticity distribution,

$$\omega(r) = \frac{\Gamma}{2\pi a^2} \exp\left(-\frac{r^2}{2a^2}\right), \tag{B.1}$$

with $r^2 = (x - x_c)^2 + (y - y_c)^2$, is used. The corresponding exact Laplacian,

$$\nabla^2_{\mathrm{e}}\omega = \frac{2\omega}{a^2}\left(\frac{r^2}{2a^2} - 1\right), \tag{B.2}$$

will serve as a reference for the comparison with an approximate value, computed using a discretization of Eq. (A.7),

$$\nabla^2_{\mathrm{a}}\omega_{ij} = 2\sum_{p,q} \frac{1}{\sigma_{\mathrm{s}}^2}(\omega_{pq} - \omega_{ij})\frac{1}{\sigma_{\mathrm{s}}^2}\eta\left(\frac{|\mathbf{x}_{ij} - \mathbf{x}_{pq}|}{\sigma_{\mathrm{s}}}\right) S_{pq}, \tag{B.3}$$

with $\eta(z) = 1/(2\pi)\exp(-z^2/2)$ and $\sigma_s^2 = (\sigma_{ij}^2 + \sigma_{pq}^2)/2$.

One considers the exponential mapping described in Section 3.6, with $\beta = 1$. The domain covered by the particles is a sector that completely bounds the disk of center $(x_{\mathrm{c}}, y_{\mathrm{c}})$ and of radius pa, so that the domain where $\nabla^2\omega$ is significant is well covered by particles.

Here, the surface of each particle is given by

$$S = \frac{\sinh(2\pi/m)}{(2\pi/m)}\left(\left(\frac{2\pi}{m}R_0\right)\cdot\exp\left(\frac{2\pi i}{m}\right)\right)^2 \triangleq h^2 = \frac{\sigma^2}{\beta^2}, \tag{B.4}$$

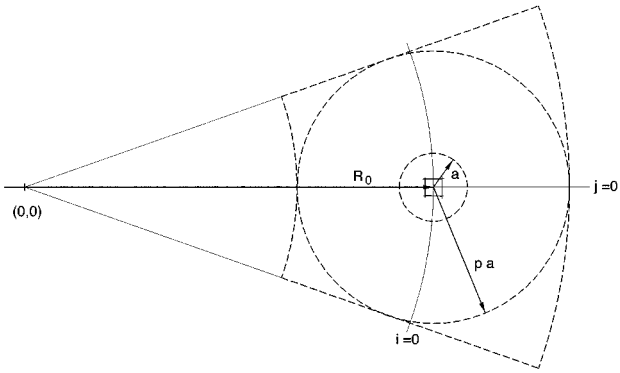

FIG. 41. Sketch of the situation for the numerical evaluation of the Laplacian of a Gaussian vortex.

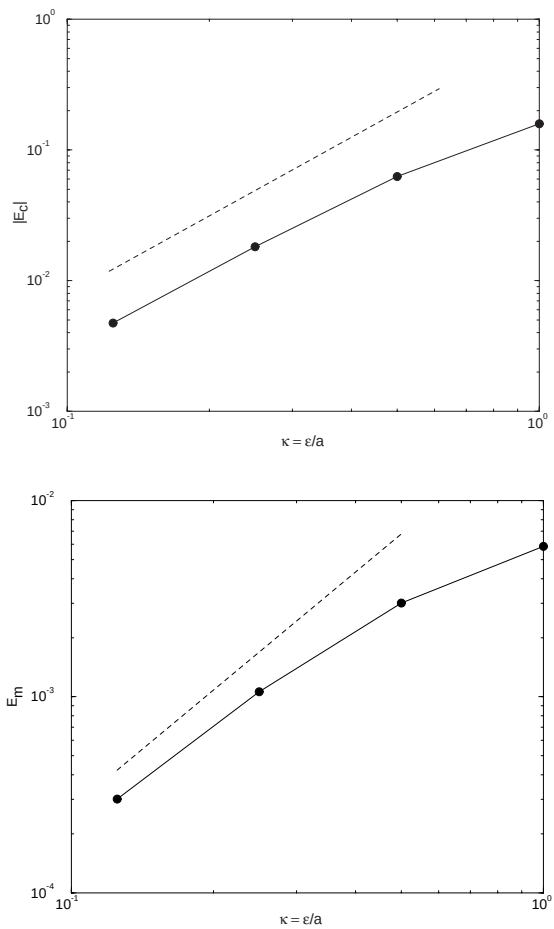

FIG. 42. Numerical approximation of the Laplacian. Top: $|E_c|$ as a function of $\kappa = \epsilon/a$ for $\delta = 2$ (dashed line has a slope of 2). Bottom: E_m as a function of $\kappa = \epsilon/a$, for $\delta = 2$ (dashed line has a slope of 2).

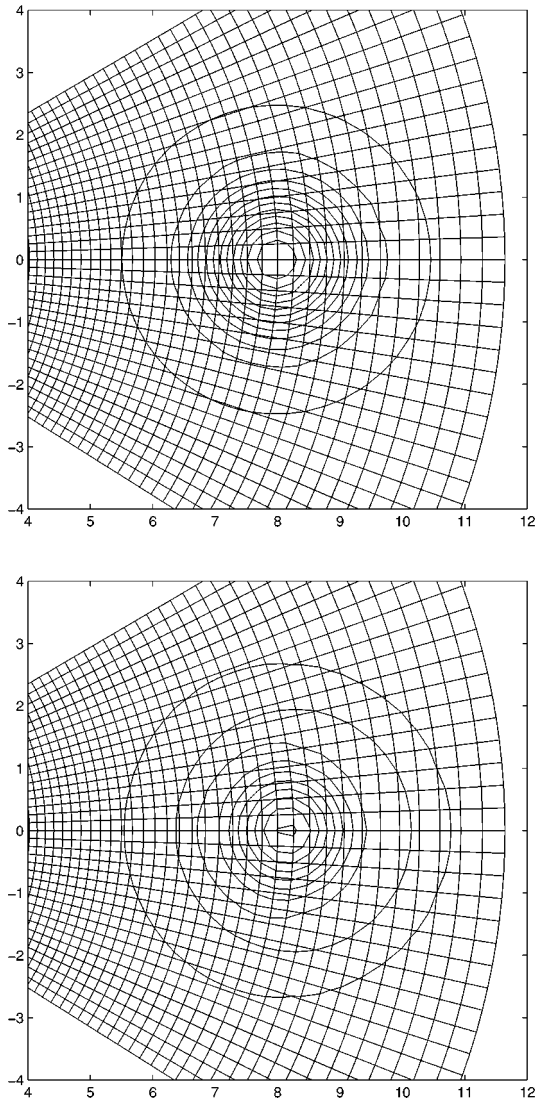

FIG. 43. Numerical approximation of the Laplacian, for $\delta = 2$ and $\kappa = 1/4$. Top: iso contours of $\nabla^2_a \omega$ (levels are by steps of 0.03) and cells of the mapping. Bottom: iso contours of $E = \nabla^2_e \omega - \nabla^2_a \omega$ (levels are by steps of 0.003) and cells of the mapping.

with $i = 0$ corresponding to $\mathbf{x}_c$ (see Fig. 41). Hence, one has

$$\sigma(i) = \beta h(i) = \beta \left(\frac{\sinh(2\pi/m)}{(2\pi/m)} \right)^{1/2} \cdot \left(\frac{2\pi}{m} R_0 \right) \cdot \exp\left(\frac{2\pi}{m} i \right)$$
$$= \beta \left(\frac{\sinh(\epsilon/R_0)}{(\epsilon/R_0)} \right)^{1/2} \cdot \epsilon \cdot \exp\left(\frac{\epsilon}{R_0} i \right), \tag{B.5}$$

with $\epsilon = \frac{2\pi}{m} R_0$. This is in the form used in Appendix A.

Two parameters are defined: $\delta = R_0/(pa)$ and $\kappa = \epsilon/a$. The first one, δ, is a measure of the distortion of the mapping over the region covered by the vortex, while κ is related to

the quality of the discretization, as it measures the ratio between cell size, h_c, at the vortex center, and physical problem size, a. The center of the vortex corresponds to $(i, j) = (0, 0)$; thus,

$$x_c = R_0 \tag{B.6}$$

$$y_c = 0. \tag{B.7}$$

Figure 41 illustrates the problem. Tests have been run for $\delta = 2$, 4, 8, 16, 32, 64 and $\kappa = 1, 1/2, 1/4, 1/8$. The vortex is normalized: $\Gamma = 1$, $a = 1$; p is set to 4, and hence the domain where $\nabla^2\omega$ is significant is here very well covered by particles. Two errors are computed for each run: the error at the center of the vortex (where it is maximum),

$$E_c = \nabla_e^2\omega\big|_{\mathbf{x}=\mathbf{x}_c} - \nabla_a^2\omega\big|_{\mathbf{x}=\mathbf{x}_c}, \tag{B.8}$$

and the mean error,

$$E_m = \frac{\sum_{i,j} \left|\nabla_e^2\omega_{ij} - \nabla_a^2\omega_{ij}\right| S_{ij}}{\sum_{i,j} S_{ij}}. \tag{B.9}$$

Figure 42 illustrates the variations of $|E_c|$ and E_m with κ for the most severe case: $\delta = 2$. It is seen that the method indeed converges as κ^2, as expected. The higher values of δ (which correspond to less severe distortions of the mapping) lead to results that are almost identical. Isocontours of $\nabla_a^2\omega$ and $E = \nabla_e^2\omega - \nabla_a^2\omega$, for the case $\delta = 2$ and $\kappa = 1/4$, are plotted in Fig. 43, together with the mapping used. It is seen that $\nabla_a^2\omega$ is almost axisymmetric and that the error, E, is also almost axisymmetric. This confirms the theoretical proof of Appendix A.

ACKNOWLEDGMENTS

P. Ploumhans was supported by Fonds pour la Formation la Recherche dans l'Industrie et dans l'Agriculture (FRIA). Part of the computer time was provided by the Action de Recherche Concertée (ARC) ARC 97/02-210 of Professors R. Keunings and V. Legat. We also thank E. Bonaffini for his help in the creation of some figures.

REFERENCES

1. M. Bar-Lev and H. T. Yang, Initial flow field over an impulsively started circular cylinder, *J. Fluid Mech.* **72**, 625 (1975).
2. J. E. Barnes and P. Hut, A hierarchical $\mathcal{O}(N \log N)$ force calculations algorithm, *Nature* **324**, 446 (1986).

2a. R. Benhaddouch, Treatment of a Neumann boundary condition by a Particle Strength Exchange method, in *Electronic Proc. Third International Workshop on Vortex Flows and Related Numerical Methods, Toulouse, August 24–27, 1998*, ESAIM (European Series in Applied and Industrial Mathematics) (1999), available at http://www.emath.fr/Maths/Vol.7/.

3. G.-H. Cottet, M. Lemine, and M. El Hamraoui, Recent developments in vortex methods for the simulation of unsteady incompressible flows, in *Electronic Proc. Third International Workshop on Vortex Flows and Related Numerical Methods, Toulouse, August 24–27, 1998*, ESAIM (European Series in Applied and Industrial Mathematics) (1999), available at http://www.emath.fr/Maths/Proc/Vol.7/.
4. G.-H. Cottet and P. Koumoutsakos, *Vortex Methods: Theory and Applications* (Cambridge Univ. Press, Cambridge, UK, 2000).
5. P. Degond and S. Mas-Gallic, The weighted particle method for convection–diffusion equations. I. The case of an isotropic viscosity; II. The anisotropic case, *Math. Comput.* **53**, 485 (1989).

6. L. Greengard and V. Rohklin, A fast algorithm for particle simulations, *J. Comput. Phys.* **73**, 325 (1987).
7. P. Koumoutsakos, *Direct Numerical Simulations of Unsteady Separated Flows Using Vortex Methods*, Ph.D. thesis, California Institute of Technology, 1993.
8. P. Koumoutsakos, A. Leonard, and F. Pépin, Boundary conditions for viscous vortex methods, *J. Comput. Phys.* **113**, 52 (1994).
9. P. Koumoutsakos and A. Leonard, High resolution simulation of the flow around an impulsively started cylinder using vortex methods, *J. Fluid Mech.* **296**, 1 (1995).
10. P. Koumoutsakos and D. Shiels, Simulations of the viscous flow normal to an impulsively started and uniformly accelerated flat plate, *J. Fluid Mech.* **328**, 177 (1996).
11. M. Lemine, *Couplage de Méthodes Numériques en Simulation Directe d'Écoulements Incompressibles*, thèse, Université Joseph Fourier, 1998.
12. A. Leonard, D. Shiels, J. K. Salmon, G. S. Winckelmans, and P. Ploumhans, Recent advances in high resolution vortex methods for incompressible flows, in *Proc. 13th AIAA Computational Fluid Dynamics Conf., Snowmass Village, CO, June 29–July 2, 1997*, AIAA #97-2108.
13. A. Leonard, Review: Vortex methods for flow simulation, *J. Comput. Phys.* **37**, 289 (1980).
14. A. Leonard, Computing three-dimensional incompressible flows with vortex elements, *Annu. Rev. Fluid Mech.* **17**, 523 (1985).

14a. S. Mas-Gallic, Particle approximation of a linear convection-diffusion problem with Neumann boundary conditions, *SIAM J. Numer. Anal.* **32**(4), 1098 (1995).

15. P. Ploumhans, G. S. Winckelmans, and J.K. Salmon, Vortex particles and tree codes. I. Flows with arbitrary crossing between solid boundaries and particle redistribution lattice; II. Vortex ring encountering a plane at an angle, in *electronic Proc. Third International Workshop on Vortex Flows and Related Numerical Methods, Toulouse, August 24–27, 1998*, ESAIM (European Series in Applied and Industrial Mathematics) (1999), available at http://www.emath.fr/Maths/Proc/Vol.7/.
16. J. K. Salmon and M. S. Warren, Skeletons from the Treecode Closet, *J. Comput. Phys.* **111**(1), 136 (1994).
17. F. Y. Wang, O. Karatekin, and J.-M. Charbonnier, An experimental study of the flow-field around an Apollo capsule at low speed, in *Proc. 36th AIAA Aerospace Sciences Meeting and Exhibit, Reno, NV, January 12–15, 1998*, AIAA #98-0319.
18. G. S. Winckelmans and A. Leonard, Contributions to vortex particle methods for the computation of three-dimensional incompressible unsteady flows, *J. Comput. Phys.* **109** (2), 247 (1993).
19. G. S. Winckelmans, J. K. Salmon, A. Leonard, and M. S. Warren, Three-dimensional vortex particle and panels methods: Fast tree-code solvers with active error control for arbitrary distributions/geometries, in *Proc. Forum on Vortex Methods for Engineering Applications, Albuquerque, NM, February 22–24*, p. 25.
20. G. S. Winckelmans, J. K. Salmon, M. S. Warren, A. Leonard, and B. Jodoin, Application of fast parallel and sequential tree codes to computing three-dimensional flows with the vortex element and boundary element methods, Applied and Industrial Mathematics), in *Electronic Proc. Second International Workshop on Vortex Flows and Related Numerical Methods, Montréal, Canada, August 20–24, 1995*, ESAIM (European Series in Industrial and Applied Mathematics) (1999), available at http://www.emath.fr/Maths/Proc/Vol.1/index.htm.